

Impact of Organics and Carbonates on the Oxidation and Precipitation of Iron during Hydraulic Fracturing of Shale

Adam D. Jew^{1,2*}, Megan K. Dustin², Anna L. Harrison^{1,2}, Claresta M. Joe-Wong², Dana L. Thomas², Katharine Maher², Gordon E. Brown, Jr.^{1,2,3}, and John R. Bargar¹

1) *Stanford Synchrotron Radiation Lightsource, SLAC National Accelerator Laboratory, 2575 Sand Hill Rd., Menlo Park, CA 94025, USA*

2) *Department of Geological Sciences, School of Earth, Energy, and Environmental Sciences, Stanford University, Stanford, CA 94305-2115, USA*

3) *Department of Photon Science, SLAC National Accelerator Laboratory, Stanford University, 2575 Sand Hill Rd., Menlo Park, CA 94025, USA*

*Corresponding Author: adamjew@stanford.edu

For Submission to Energy & Fuels

Abstract:

Hydraulic fracturing of unconventional hydrocarbon reservoirs is critical to the United States energy portfolio; however, hydrocarbon production from newly fractured wells generally declines rapidly over the initial months of production. One possible reason for this decrease, especially over time scales of several months, is the mineralization and clogging of microfracture networks and pores proximal to propped fractures. One important but relatively unexplored class of reactions that could contribute to these problems is oxidation of Fe(II) derived from Fe(II)-bearing phases (primarily pyrite, siderite, and Fe(II) bound directly to organic matter) by the oxic fracture fluid and subsequent precipitation of Fe(III)-(oxy)hydroxides. The extent to which such reactions occur and their rates, mineral products, and physical locations within shale pore spaces are unknown. To develop a foundational understanding of potential impacts of shale iron chemistry on hydraulic stimulation, we reacted sand-sized (150-250 μm) and whole rock chips (cm-scale) of shales from four different formations (Marcellus Fm., New York; Barnett Fm., Central Texas; Eagle Ford Fm., Southern

1 Texas; and Green River Fm., Colorado) at 80°C with synthetic fracture fluid, with and without
2 HCl. These four shales contain variable abundances of clays, carbonates, and total organic
3 carbon (TOC). We monitored Fe concentration in solution and evaluated changes in Fe
4 speciation in the solid phase using synchrotron-based techniques. Solution pH was the most
5 important factor affecting the release of Fe into solution. For reactors with an initial solution
6 pH of 2.0 and low carbonate content in the initial shale, the sand-sized shale showed an initial
7 release of Fe into solution during the first 96 hours of reaction, followed by a plateau or
8 significant drop in solution Fe concentration, indicating that mineral precipitation occurred. In
9 contrast, in reactors with high pH buffering capacity, little to no Fe was detected in solution
10 throughout the course of the experiments. In reactors that contained no added acid (initial pH
11 = 7.1), there was no detectable Fe release into solution. The carbonate-poor whole rock
12 samples showed a steady increase, then a plateau in Fe concentration during 3 weeks of
13 reaction, indicating slower Fe release and subsequently slower Fe precipitation. Synchrotron-
14 based x-ray fluorescence mapping coupled with x-ray absorption spectroscopy (both bulk and
15 micro) showed that when solution pH was above 3.25, Fe(III)-bearing phases precipitated in the
16 shale matrix. Initially, ferrihydrite precipitated on and in the shale, but as experimental time
17 increased, the ferrihydrite transformed to either goethite (at pH 2.0) or hematite (pH > 6.5).
18 Additionally, not all of the released Fe(II) was oxidized to Fe(III), resulting in precipitation of
19 mixed-valence phases such as magnetite. Idealized systems containing synthetic fracture fluid
20 and dissolved ferrous chloride but no shale showed that in reactors open to the atmosphere at
21 low pH (< 3.0), Fe(II) oxidation is inhibited. Surprisingly, the addition of bitumen, which is often
22 extracted by organic compounds in the fracture fluid, can override this inhibition of Fe(II)
23 oxidation caused by low pH. Nonetheless, O₂ in the system is still the most important factor
24 controlling Fe(II) oxidation. These results indicate that Fe redox cycling is an important and
25 complex part of hydraulic fracturing and provide evidence that Fe(III)-bearing precipitates
26 derived from oxidation of Fe(II)-bearing phases could negatively impact hydrocarbon
27 production by inhibiting transport.

1 **Introduction:**

2 Hydraulic fracturing in the United States has seen a strong increase in both the number of new
3 wells being drilled and the re-fracturing of oil/gas shales that were previously hydraulically
4 fractured¹. Although hydraulic fracturing is positively impacting the energy landscape of the
5 United States, production drops significantly within several months of initial hydrocarbon
6 production²⁻⁸. The majority of modeling efforts examining declines in production of gas have
7 focused on changes to advective flow due to a reduction in the subsurface pressure gradients
8 caused by extraction⁸. Modeling results are generally consistent with initial production data
9 provided by field operators; however, the discrepancy between model predictions and
10 observations increases over time⁸. One possible cause for the late-stage model discrepancy
11 and decrease in hydrocarbon production in these systems is the precipitation of minerals that
12 can occlude pores, pore throats, fractures, and piping used during the fracturing process. There
13 is a substantial amount of reduced Fe in oil/gas shales, and precipitation of Fe-bearing phases is
14 known to be problematic in hydraulic fracturing⁹. Various Fe-controlling agents are added to
15 the fluids injected into the subsurface, including citric acid, ethylene glycol, acetic acid,
16 thioglycolic acid, and sodium erythorbate¹⁰. Although these chemicals, coupled with corrosion
17 inhibitors, have been shown in simplified laboratory studies to inhibit the release of Fe
18 (corrosion inhibitor) and the precipitation of Fe(III)-(oxy)hydroxides (Fe-controlling agent),
19 produced water from hydraulic fracturing commonly contains significant quantities of Fe
20 (including suspended crystalline Fe-bearing phases) in solution, indicating that the Fe-
21 controlling agents in the subsurface do not eliminate Fe release into solution¹¹⁻¹⁷. Due to the
22 small size of fractures and pores in the subsurface rocks (ranging from nm's to mm's in
23 diameter), even a small amount of Fe(III)-bearing precipitate has the potential to have a large
24 impact on permeability¹⁸⁻²⁵. A detailed investigation of Fe cycling in hydraulically fractured
25 shales is required to determine the extent to which precipitation of Fe(III)-bearing solids does
26 indeed occur and the chemical controls that govern this process.

27 To address these needs, as well as to determine if Fe-controlling agents do inhibit the formation
28 of Fe(III)-precipitates in oil/gas shale systems, experiments were conducted in which shales
29 from four different shale formations were reacted with synthetic hydraulic fracture fluid. The
30 four shales chosen for study [Marcellus (New York), Barnett (Central Texas), Eagle Ford (South
31 Texas), and Green River (Colorado)] offer a wide range of differences in carbonate, clay, and
32 organic contents as well as in kerogen types. The focus of the present study is to determine: (1)
33 which chemical processes are primarily responsible for Fe release from the shales, (2) which
34 factors contribute to Fe(II) oxidation, and (3) the identity and locations of Fe-bearing solid
35 phases before and after reaction with synthetic hydraulic fracture fluid. A combination of wet
36 chemical, x-ray diffraction (XRD), and synchrotron-based imaging and x-ray absorption
37 spectroscopic techniques was used to determine changes in Fe speciation throughout the

1 experimental process and provided valuable insights about the potential role of Fe(III)-bearing
2 precipitates in limiting hydrocarbon production from hydraulically fractured shale systems. In
3 addition, the experimental results help identify possible areas in which improvements to the
4 hydraulic fracturing process can be achieved. This paper is a companion to a paper that used
5 the sand-sized shale experiments to explore the controls on mineral dissolution, not limited to
6 Fe-phases, and the implications of mineral-fluid reaction on porosity changes and the release of
7 heavy metal contaminants from shale systems (Harrison *et al.*, *in press*). Here, we focus solely
8 on the dynamics of Fe-cycling, and present additional experimental results that help us assess
9 the role of organics on Fe-cycling.

10 These experiments were designed to examine chemical reactions that occur in shale pore space
11 at the onset of fracture fluid-shale reactions, prior to and during neutralization of acid. The
12 crucial time period for these reactions is between 1 and 10 days because most shale alteration
13 occurs in this interval. Acid is generally injected into formations within a few hours, before acid
14 neutralization can occur. Consequently acid-driven shale alteration is expected to be
15 widespread within new stimulated fractures. The salinity of shale pore fluids during these early
16 times is expected to be controlled by the composition of the injected fluid and the solid phases
17 present and not by TDS present in flowback or produced water. Flowback does not occur until
18 much later, when the well is unplugged, typically after several weeks. For this reason, our
19 experiments cannot be compared directly to flowback water conditions.

20 **Methods**

21 **Shale Samples:**

22 Samples from the Marcellus shale (Oatka Creek Member, New York), Eagle Ford shale (South
23 Texas), Barnett shale (Central Texas), and Green River shale (Mahogany Ledge Member,
24 Colorado) were selected for experimentation due to their significant differences in clay,
25 carbonate, and organic matter contents. Although there are significant variations in mineralogy
26 in each of the different shales (*i.e.* Marcellus shale contains regions with high carbonate and
27 low clay as well as regions with low carbonate and high clay), samples were selected in order to
28 investigate a wide range of differing shale mineralogies. The Marcellus shale (GPS: Lat. 42.98,
29 Long. -77.99) and Green River shale (GPS: Lat. 39.58, Long. -107.89) samples used were outcrop
30 samples collected in July 2016 and August 2015, respectively. Barnett and Eagle Ford samples
31 are core samples taken at depth (2613 m and 3915 m, respectively). Due to proprietary
32 information involving the Eagle Ford and Barnett shale samples, their sample localities can not
33 be divulged in this work.

34 **Fracture-Fluid Composition:**

1 The fracture fluid recipe used in these experiments (**Table 1**) is similar to that used in the
2 National Energy Technology Laboratory's (NETL) Marcellus Well E in Greene County, PA²³.
3 Because the present study focuses on the release of Fe from shale, silica proppants were not
4 included in the reactors. Additionally, due to the very low quantities of two biocides (2,2-
5 dibromo-3-nitrilopropionamide and dibromoacetonitrile) compared to polyethylene glycol, the
6 additional biocides were not used in our fracture fluid formulation. After a comparison
7 between the chemical recipe used by NETL and other recipes employed in the Marcellus region,
8 using the FracFocus online database¹⁰, we chose the recipe outlined in **Table 1** as a reasonable
9 approximation of fracture fluid for this region. Though not every hydraulic fracturing operation
10 uses HCl, either for well bore cleaning or throughout the injection process, it is used in a
11 significant proportion of operations (> 55% nationwide and nearly 100% in carbonate-rich
12 shales)¹⁰. The largest difference between the composition of this fluid and those used in the
13 Texas region (Eagle Ford and Barnett) is the replacement of ethylene glycol used in cold
14 weather regions, such as the Marcellus Shale, with methanol as the main solution corrosion
15 inhibitor. Because methanol and ethylene glycol are generally considered to have similar
16 binding affinities for iron, using the Marcellus fracture fluid for Eagle Ford and Barnett samples
17 is not expected to change the reaction mechanism and reaction products in a significant way.
18 In an industrial setting, different chemicals are injected at different times over a 12-hour period
19 and in general are left for a period of 3 weeks prior to extraction. Given the long time frame of
20 the experiments, the impracticality in doing multiple chemical injections, and the strong
21 likelihood of mixing in the subsurface, all chemicals for the fracture fluid were mixed together
22 prior to addition to reactors and introduced to the shale samples all at once. The final pH of the
23 solution with all chemicals added, including HCl, was pH = 2.0.

24 **Bitumen Extraction:**

25 Chemicals common to almost all fracture fluids⁴ have the ability to extract bitumen from oil/gas
26 shales in the field, with dibromoacetonitrile and 2-ethyl hexanol being the dominant
27 extractants^{26, 27}. Use of these additives will therefore result in liberation of bitumen within the
28 shale pores and fracture space, with the possibility of subsequent reaction with Fe. To study
29 the impact of bitumen on iron cycling dynamics, bitumen was extracted from Marcellus and
30 Green River shale samples for use in idealized Fe systems described later by following the first
31 two extraction steps outlined by Göklen *et al.*, which were designed to extract kerogen from
32 the Green River Shale²⁸. The first step consists of reaction of the shale with a 3N hydrochloric
33 acid (HCl) solution at 70°C to remove carbonates. The second step, designed to remove
34 bitumen, utilizes a Soxhlet extractor charged with 3:1 toluene to methanol. After bitumen was
35 extracted, the toluene/methanol solution containing bitumen was placed in a desiccator
36 connected to a vacuum pump that vented into a fume hood to remove the high vapor pressure
37 toluene and methanol and leave behind the bitumen for use in our bitumen/Fe experiments.

1 **Shale/Fracture Fluid Reactors:**

2 Experiments consisted of 3-week, 3-month, and 6-month long reactions performed in 250 mL
3 glass bottles with butyl-rubber stoppers that were partially permeable to O₂. Experiments were
4 also conducted with an Ar-filled headspace (125 mL bottles) with thicker butyl-rubber stoppers
5 to eliminate O₂ intrusion. All glassware was acid washed, triple rinsed in double deionized (DDI)
6 water (18.2 MΩ), and heated in a furnace overnight at 700°C. To remove any leachable
7 organics from the butyl-rubber stoppers, both types of stoppers were immersed in boiling 0.1
8 M KOH for one hour and then triple rinsed in DDI water prior to use.

9 The 250 mL reactors were filled with 1 g of shale material, either sand-sized particles (250-350
10 μm) or shale chips (0.5-1 cm), and 200 mL of fluid, resulting in 50 mL of headspace. The shale
11 material consisted of Marcellus, Eagle Ford, Barnett, or Green River samples. Additionally,
12 corundum (α-Al₂O₃) chips were added to reactors to act as substrates for secondary mineral
13 precipitation. The fluid compositions added to reactors were varied as follows: (1) synthetic
14 fracture fluid with added HCl; (2) fracture fluid with no HCl; (3) DDI water only; and (4) HCl only.
15 The solutions and headspace were not sparged with inert gas, resulting in solutions and
16 headspaces that were initially at equilibrium with the atmospheric gases at 20°C. Injected fluids
17 in hydraulic fracturing operations are often at equilibrium with the atmosphere making the
18 unsparged reactors with Ar headspace the closest analog to real-world systems. Though the
19 unsparged reactors with air as headspace contains slightly elevated O₂ concentrations
20 compared to real-world systems, the end result would be a slight increase in the amount of
21 Fe(II) oxidation versus the Ar headspace reactors. Dissolved oxygen in produced waters is high
22 (5-10 mg/L dissolved O₂)²⁹. Sealed reactors were incubated in a convection oven at 80°C.

23 The smaller 125 mL bottles had the same solid/liquid/headspace ratio as in the 250 mL reactor
24 bottles (0.5 g shale, 100 mL fluid, and 25 mL headspace). Because these smaller reactors were
25 used to investigate the effect of O₂ in the fluid and headspace, the fluid and/or the headspace
26 were purged with ultra-high purity Ar. Sealed reactors were incubated in a convection oven at
27 80°C.

28 **Bitumen/Fe Oxidation Experiments:**

29 The main goal of these experiments was to determine the following: (1) if Fe(II) oxidation
30 occurs in shales under various pH conditions, (2) if any fracture fluid components could
31 enhance aqueous Fe(II) oxidation, and (3) if bitumen enhances aqueous Fe(II) oxidation.
32 Experimental reactors containing 40 ppm dissolved Fe(II) in the form of FeCl₂ were used to
33 determine the effect of fracture fluid, pH, O₂, and bitumen on the oxidation of Fe(II).

1 Fracture fluid was synthesized without HCl. To minimize the possibility of photo-induced
2 oxidation of Fe(II) in the reactors, all reactors were wrapped in Al foil prior to the addition of
3 any solution. For samples open to the atmosphere, 250 mL bottles were filled with 200 mL of
4 solution so that aqueous samples could be taken throughout the experiment while leaving
5 enough potential Fe(III)-containing precipitate in the bottle for later XRD analysis. For reactors
6 containing added bitumen (derived from Marcellus or Green River), the total concentration of
7 bitumen was set at 40 ppm. The bitumen concentration selected for these reactors is the
8 average of the theoretical bitumen concentrations released from Marcellus and Green River
9 shales based on the solubility of bitumen in 2-ethyl-1-hexanol²⁷, and the total amount of
10 bitumen contained in the rock samples. Additionally, 40 ppm bitumen provided a 1:1
11 Fe:Bitumen molar concentration which is a reasonable ratio for the Marcellus shale. Though pH
12 should have little to no effect on bitumen solubility^{27,30,31}, the initial pH for the reactors was set
13 at either 2.0 or 7.1 to determine the effect of pH on Fe(II) oxidation in the presence of bitumen.
14 For reactors with excess O₂, the fluid was allowed to freely exchange with the laboratory
15 atmosphere. For de-oxygenated reactors, a total of 100 serum bottles (20 mL capacity)
16 containing 10 mL of solution were prepared. Samples were incubated at 80°C and sacrificed at
17 0, 2, 5, 8, 17, 24, and 48 hours. In order to limit any addition of O₂ into Ar-sparged reactors,
18 sampling via needle and syringe of serum bottles was limited to one time only. After all
19 components were added to the serum bottles and de-oxygenated (if necessary), a de-
20 oxygenated solution of FeCl₂ was added to the vials via syringe to reach a final aqueous Fe(II)
21 concentration of 40 ppm. The cleaning procedure for the serum bottles was the same as
22 described earlier. In the de-oxygenated reactors the fracture fluid and serum bottles were
23 sparged with ultra high purity Ar. Sampling and Fe analysis of the samples are described below.

24 **pH and Fe Sampling and Analysis:**

25 Reactor experiments lasting a total of 3 weeks were sampled at 0, 6, 12, 24, 48, 96, 192, 384,
26 and 504 hours. The 3-month reactors were sampled every 10 days for a total of 90 days, while
27 the 6-month reactors were sampled every 20 days over a total period of 180 days.

28 At each time point, 5 mL of solution was taken from each reactor via needle and syringe with
29 minimal agitation to the reactor bottles. The solution was filtered through a 0.2 μm
30 polyethersulfone (PES) syringe filter into a 15 mL polypropylene centrifuge tube. Following
31 sampling, the butyl-rubber stoppers were sealed with silicone to minimize gas leakage through
32 areas of the stopper that the needle punctured, and the bottles were returned to the oven.
33 Measurements of pH, Fe(II) concentration, and total Fe concentration were carried out
34 immediately following sampling and filtration. Iron(II) and total iron concentrations were
35 determined using Ferrozine and hydroxylamine hydrochloride, respectively, with absorbance

1 being measured using a Hewlett-Packard model 8452 photo diode array UV/Vis
2 spectrophotometer at a wavelength of 562 nm.

3 **Bulk XRF Measurements:**

4 Total elemental compositions of the shale were measured using x-ray fluorescence (XRF)
5 analysis in the Stanford Environmental Measurements Laboratory. The shale samples were
6 analyzed using a Spectro Analytical XRF model XEPOS HE. A standard reference material, NIST
7 SRM 2710a (Montana soil), was analyzed in addition to our shale samples to confirm the
8 accuracy of the technique.

9 **FIB-SEM Imaging:**

10 Pyrite framboids in the Marcellus shale were imaged at the Stanford Nano Shared Facility using
11 a FEI Strata 235DB DualBeam Focused Ion Beam-Scanning electron microscope (FIB-SEM) with
12 an operating voltage of 5.0 kV.

13 **Dynamic Light Scattering Measurements:**

14 The particle size of the bitumen extracted from the Marcellus shale was measured using a
15 Malvern Zetasizer model Nano-ZS. Bitumen was suspended in DDI water and measured in a
16 quartz cuvette for a total of 40 scans.

17 **X-ray Diffraction Measurements:**

18 Bulk mineralogy of the shale samples and idealized Fe reactors was determined by x-ray
19 diffraction (XRD). Powdered samples were analyzed on a Rigaku model CM2029 powder x-ray
20 diffractometer using a Cu K α x-ray source over a 2 θ range of 5-70 $^\circ$, and data were analyzed
21 using the JADE diffraction software package³². Peak identification was accomplished by
22 matching the four most intense diffraction peaks for a given mineral to diffraction patterns in
23 the National Institute of Standards and Technology (NIST) database. In addition to mineral
24 identification, the JADE software was used for quantitative analysis of the different phases by
25 least squares fitting of the data; NIST diffraction patterns of reference compounds were used to
26 fit the diffraction patterns of the samples.

27 **Synchrotron-Based X-ray Spectroscopy and X-ray Fluorescence Imaging:**

28 Unreacted and reacted samples of Barnett, Marcellus, Eagle Ford, and Green River shales were
29 analyzed using synchrotron-based micro-x-ray fluorescence (μ -XRF) mapping and μ -X-ray
30 Absorption Near Edge Structure (μ -XANES) spectroscopy on beamline 2-3 at the Stanford
31 Synchrotron Radiation Lightsource (SSRL). Beamline 2-3 consists of a bending magnet insertion
32 device using two water-cooled Si(111) monochromator crystals in the $\Phi = 90^\circ$ orientation to

1 select x-ray energy. Both μ -XRF maps and μ -XANES spectroscopy data were collected using a
2 three-element vortex detector in fluorescence mode. The beam energy was set to 15 keV with
3 a 2 μm x 2 μm beam size. The detection limit was approximately 50 ppm per pixel for each
4 elemental map collected. Regions with high Fe content were chosen for Fe μ -XANES data
5 collection. Iron K-edge μ -XANES spectra were collected from 250 eV below to 400 eV above the
6 Fe K-edge (7112 eV). Energy calibration was done using an Fe metal foil placed behind the I_1
7 ion chamber. Multiple energy maps at 7122, 7128, and 7133eV were collected to determine
8 the spatial distribution of Fe(II) versus Fe(III). Descriptions of data analysis for μ -XRF and μ -
9 XANES data are given in the next subsection.

10 Bulk fluorescence yield Fe K-edge EXAFS spectra for the shale samples were collected on SSRL
11 beamline 4-1, which has a wiggler insertion device and uses two water-cooled Si(220)
12 monochromator crystals in the $\Phi = 0^\circ$ orientation. Extended X-ray Absorption Fine Structure
13 (EXAFS) data were collected in fluorescence yield mode using a passivated implanted planar
14 silicon detector. An Fe-metal foil was inserted between the second and third ion chambers for
15 continuous energy calibration. Samples were maintained at 77K using a LN₂ cryostat during
16 EXAFS data collection to reduce thermal disorder and make second-neighbor atoms easier to
17 detect. Three scans were collected for all samples with a maximum k -range of 15 \AA^{-1} .

18

19 **X-ray Absorption Spectroscopy and X-ray Fluorescence Imaging Analysis:**

20 The μ -XRF maps were processed and analyzed using the SMAK³³ software package, whereas
21 bulk EXAFS and μ -XANES spectra were analyzed using the SixPACK^{34, 35} software package. Both
22 μ -XANES and EXAFS spectra were fit by linear combination fitting (LCF) using previously
23 collected x-ray absorption spectra (XAS) of various Fe-bearing compounds. μ -XANES data were
24 fit from 100 eV below to 350 eV above the Fe K-edge. Due to issues with glitches in the EXAFS
25 data, the EXAFS data were fit from $k = 3$ to $k = 12 \text{\AA}^{-1}$. Goodness-of-fit was determined by
26 calculating the residual of the fit using one-component or multi-component fits and the
27 following formula, where v represents the $k^3 \chi(k)$ value of the EXAFS data:

$$\text{Residual} = \frac{\sum_{t=1}^n (v_{\text{data}} - v_{\text{fit}})^2}{n}$$

28

29 Shell-by-shell fitting of the data was used to identify an oscillation in the EXAFS data that could
30 not be fit with inorganic Fe reference compounds currently in our spectrographic reference
31 library. More than 30 single-scattering pathways for Fe-O, Fe-C, Fe-S, Fe-B, Fe-N, Fe-CN, Fe-
32 NO₃, Fe-SO₃, and Fe-SO₄ of varying backscatterer distances were created using literature data

1 for typical Fe(II)-X distances in organo-metallic molecules³⁶ and the single-scattering pathway
2 generation module in the SixPACK software package using FEFF 6L^{34, 35, 37}.

3 **Results:**

4 **Impact of Fracture Fluid on Shale Mineralogy** - The four shales used in this work had large
5 variations in clay, carbonate, pyrite, and organic contents. The Barnett shale contains the
6 highest clay content (40.6 wt.%) of the four shales, followed by Marcellus, Oatka Creek, (35.0
7 wt.%), Eagle Ford (7.6 wt.%), and Green River, Mahogany Ledge (<1 wt.%) (**Table 2**). By
8 definition, the Green River Shale samples used are not true shales because of the lack of
9 significant quantities of clays; however, we will continue to use the term Green River Shale due
10 to the historical use of this term for the Green River formation. As seen in **Table 2**, the Barnett,
11 Marcellus, and Green River shales have illite as the dominant clay mineral. The dominant clay
12 mineral in the Eagle Ford shale is kaolinite. Carbonate mineralogy (**Table 2**), which is a good
13 indicator of the pH buffering capacity of a rock, differs significantly among the shale samples,
14 with Eagle Ford having the highest carbonate content (64.5 wt.%), followed by Green River
15 (54.6 wt.%), Marcellus (12.7 wt.%), and Barnett (8.2 wt.%). Calcite is the dominant carbonate
16 mineral found in the Marcellus, Eagle Ford, and Barnett samples (> 80%), with minor amounts
17 of dolomite. The Green River shale contains significant dolomite (28.9 wt.%) as well as calcite
18 (23.2 wt.%) (**Table 2**).

19 Quantitative XRD results (**Table 2**) show a high consistency between duplicate samples
20 along with distinct trends in mineralogy with reaction time. Throughout the reaction of the
21 Marcellus samples, pH rose from the initial pH = 2.0 (**Figure 1**) to pH = 3.4. Neutralization of the
22 acidic fracture fluid is reflected in the lack of detectable carbonate minerals post-reaction
23 (**Table 2**). Throughout the reaction time there was a significant increase in the illite content
24 from an initial concentration of 35.0 wt.% to 43.8 wt.% at the end of 6 months. During the
25 same time period, the concentration of pyrite decreased from an initial value of 6.4 wt.% to a
26 final value of 4.2 wt.%, indicating significant pyrite dissolution and release of Fe(II) into solution.
27 Barnett samples showed the least amount of alteration throughout the entire 6-month
28 experimental period as indicated by both the lack of change in mineralogy (**Table 2**) and the
29 lack of any significant neutralization of the acidic solution (**Figure 1**). Unlike the Marcellus and
30 Barnett samples where all the carbonate was lost during reaction, the Eagle Ford and Green
31 River samples still contained significant quantities of carbonates even after 6 months of
32 reaction. As indicated by pH measurements (**Figure 1**), reaction of the fracture fluid with the
33 shale caused the pH of the fracture fluid to increase from 2.0 to > 6.0 within the first 48 hours
34 of reaction and then the pH stabilized for the remainder of the experimental time. The
35 concentration of carbonate minerals remaining in both the Eagle Ford and Green River samples
36 was still > 50 wt.% following reaction in all experiments. In the case of the Green River shale,

1 calcite was preferentially dissolved relative to dolomite. Comparison of quantitative XRD
2 results before and after 3 weeks of reaction of the shale samples often shows an increase in the
3 overall concentrations of quartz and pyrite. This increase is due to re-normalization of the
4 remaining phases following the removal of significant quantities of carbonate minerals from the
5 shale samples because of dissolution (**Table 2**). Similar to the Marcellus shale, there is a
6 detectable decrease in pyrite concentration in the Eagle Ford sample from 4 wt.% after 3 weeks
7 of reaction time to 2.8 wt.% after the 6 months of reaction time. Although pyrite was not
8 detectable by XRD in the Green River samples, there is abundant pyrrhotite in these samples as
9 shown by synchrotron XRF mapping coupled with μ -XANES and bulk EXAFS spectroscopy as
10 discussed below.

11 **Changes in Bulk Sample Composition** - A list of major and selected trace elements in the shales
12 before and after reaction with fracture fluid is presented in **Table 3**. Total iron in the solid
13 samples for Marcellus and Barnett shales dropped significantly with reaction time (**Table 3**).
14 Marcellus shale had an initial Fe concentration of 45.63 mg/g that dropped by ~5 mg/g or more
15 throughout the course of reaction. Similar to the Marcellus shale experiments, the Barnett
16 shale experiments also showed a loss of Fe from the solid samples from an initial concentration
17 of 24.8 mg/g to less than 21.8 mg/g for all incubation times. Eagle Ford and Green River shales
18 show no consistent trend for Fe concentrations with time. In the reactors for all four shales,
19 there was a drop in total Ca in the solid material due to calcite dissolution. Total Ca
20 concentrations in the Barnett and Marcellus shale reactors both decrease from initial
21 concentrations of 4.2 wt.% (Marcellus) and 2.5 wt.% (Barnett) to below 0.2 wt.% by 3 months
22 (**Table 3**). Although the Eagle Ford and Green River shales did show a decrease in total Ca
23 concentrations at the end of 6 months of reaction, both shales still contained over 9 wt.% Ca.
24 Of all the shale types, the Barnett shale was the only one that showed a significant reduction in
25 carbon throughout the course of the experiments. This initial concentration of C in the
26 unreacted shale was 16 wt.% and decreased to below 5 wt.% upon reaction with the fracture
27 fluid. For all four shale types, Na and K showed little to no change throughout the experiments.
28 Although there is variability in Al and Si in the reactors, because the shale samples were reacted
29 in borosilicate glass containers with a corundum chip, it is difficult to ascertain if variations in
30 elemental concentration are derived from changes in the shale or from the reaction
31 vessel/corundum chip.

32 **Evolution of Solution Composition** - The carbonate content of the unreacted shale samples is
33 the primary control on the pH of the shale-fracture fluid systems with time (**Table 2 and Figure**
34 **1**). In reactor experiments that included HCl, the starting pH was 2.0, but as reaction time
35 increased, the pH in the Eagle Ford and Green River shale reactors increased to > 6.0, whereas
36 the pH for the Barnett and Marcellus shale reactors rose only to 3 to 4. In all reactors that
37 contained no HCl (3-week, 3-month, and 6-month), little to no Fe was released into solution as

1 shown in **Figure 2** for the sand-sized Marcellus samples. In reactors containing fracture fluid
2 and HCl, Marcellus and Barnett shale samples showed a significant increase in Fe released into
3 solution, followed by a decrease, suggesting precipitation of one or more Fe-bearing phases or
4 sorption of Fe onto another solid. Under all experimental conditions examined for the
5 Marcellus and Barnett shales, the Fe(II) and Fe_{tot} concentrations follow the same trends, with
6 Fe_{tot} being slightly higher in concentration, indicating the presence of dissolved or colloidal
7 Fe(III). In the case of the Eagle Ford and Green River shale samples, which contain > 50 wt.%
8 carbonates, there was little to no detectable Fe in solution (**Figure 2**). The Fe solution data for
9 Marcellus and Barnett whole shale chips show a highly retarded Fe release when compared
10 with the sand-sized particles due to the lower surface area per unit mass of the large chips.
11 Both the Eagle Ford and Green River whole shale chip reactors had no detectable Fe in solution,
12 which is similar to our findings for the sand-sized Eagle Ford and Green River samples.

13 **Iron Mineralogy Evolution at the Micron Scale** – Micro-XRF mapping and Fe K-edge μ -XANES
14 spectroscopy were conducted in order to image Fe distribution and determine Fe speciation on
15 micron scales on single sand-sized shale grains. This approach is preferred rather than using
16 bulk XAS techniques, which provide speciation information averaged over hundreds of sand-
17 sized particles. The x-ray beam for μ -XRF imaging penetrates over 30 μ m into the sample,
18 providing imaging and speciation information for the surface of particles as well as into the
19 shale matrix. The Fe(II) and Fe(III) maps of the unreacted samples for all four shales are shown
20 in **Figure 3**. Multiple-energy XRF mapping of the unreacted sand-sized shale samples of all four
21 shale types below and above the Fe K-edge shows minor amounts of Fe(III)-bearing phases
22 around the margins of Fe(II)-bearing particles in the samples. μ -XANES analysis of Fe(II) hot
23 spots in the Barnett, Marcellus, and Eagle Ford shales shows that they are pyrite (**Figure 3**).
24 Scanning electron microscopy (SEM) shows that these grains have a dominantly framboidal
25 texture, consistent with pyrite morphology (**Figure 4**). Although the particles such as in **Figure 3**
26 are exclusively pyrite in the Barnett, Marcellus, and Eagle Ford shales, other pyrite framboids
27 examined in these samples often contained a mixture of pyrite and magnetite. In contrast, μ -
28 XANES analysis of the Fe(II) hot spots in the Green River shale shows that the primary Fe(II)-
29 sulfide is pyrrhotite rather than pyrite. Additionally, analyses of the μ -XANES spectra of Fe-rich
30 particles in the Green River samples indicate Fe(III) in goethite, ilmenite, potassium feldspar, as
31 well as trace amounts of hematite.

32 The pyrite content of the shales, which ranges from 2.1 to 6.4 wt.% (**Table 2**), is the
33 largest source of inorganic Fe and is therefore one of the most important variables with regard
34 to iron cycling in these shales. Based on XRD and XRF results (**Tables 2 and 3**), pyrite in these
35 samples comprises $\geq 90\%$ of the total initial inorganic Fe pool, with additional iron from siderite
36 and clays; however, XRF mapping and μ -XANES spectroscopy also showed the presence of
37 magnetite in all four shales. In addition, pyrrhothite is the only iron sulfide detected in the

1 Green River samples. In all of the unreacted shale samples investigated, regardless of whether
2 the samples are outcrop or core samples, some Fe(III) is present as shown in **Figure 3**. μ -XANES
3 analyses of the Fe(III)-rich areas indicate that the main Fe(III)-bearing phase present in all four
4 sample types is magnetite, although Fe(II) is still the dominant form of iron in the unreacted
5 shales.

6 Following reaction with fracture fluid, a significant amount of Fe in Marcellus shale
7 (**Figure 5**) and Eagle Ford shale (**Figure 6**) is redistributed as Fe(III)-bearing precipitates. This
8 finding indicates that Fe(II) released from the pyrite as a result of reaction with the acidic
9 fracture fluid was oxidized and precipitated as Fe(III)- and Fe(II/III)-bearing phases. Although
10 Fe(III)-bearing precipitates are spatially associated with Fe(II) hot spots in the Green River and
11 Eagle Ford samples (**Figures 5 and 6**), Fe(III) in the Marcellus and Barnett samples (data not
12 shown) is diffuse and spread out over the particle. In the case of the Eagle Ford and Green River
13 samples, Fe(III) occurs in discrete zones that are tens of microns in diameter. μ -XANES spectra
14 were collected at numerous locations for all four shale samples, and the results for the
15 Marcellus and Eagle Ford shales are presented below.

16 Because of the economic importance and significant differences between the Marcellus
17 and Eagle Ford shales, we focused our μ -XANES study on these two samples. For both, μ -XANES
18 spectra were collected around pyrite grains, which revealed varying concentrations of Fe(II) and
19 Fe(III) (**Figures 5 and 6**). The Marcellus sample contains distinct regions that are Fe(II) rich
20 (**Figure 5A**). As illustrated in **Figure 5C**, there is a significant change in the shape of the μ -XANES
21 spectra as the proportion of Fe(II) to Fe(III) changes. The XANES spectra of numerous Fe(II)-,
22 Fe(II/III)-, and Fe(III)-bearing phases were used in the linear combination fitting of these μ -
23 XANES spectra as seen in **Figures 5C and 5D**. In the Marcellus sample, the location (Spot 1) with
24 the highest Fe(II) concentration was found to be predominantly pyrite (86%), with minor
25 amounts of magnetite (14%) (**Figures 5A and 5D**). As Fe(II) concentrations decrease and Fe(III)
26 concentrations increase, ferrihydrite and goethite were detected (**Figures 5B and 5D**).
27 Magnetite was detectable in all four spots analyzed, indicating that not all of the Fe released
28 from the pyrite framboids was fully oxidized prior to precipitation. Although magnetite was
29 detected in unreacted samples, the amount and distribution differ from those of the reacted
30 samples. In the unreacted samples the magnetite is lower in concentration and closely
31 associated with the edges of pyrite grains. In contrast, in reacted samples the magnetite is
32 intermixed with the pyrite grains (**Figures 5 and 6**) or hematite (**Figure 6**). The association of
33 magnetite with the Fe(III)-oxides and pyrite was not seen in any of the unreacted samples.
34 Reacted Eagle Ford shale samples showed even more pronounced Fe(III) mineral production,
35 with the presence of large crystals (20-90 μ m in diameter) that were not detectable in the
36 unreacted shale (**Figures 6A and 6B**). As seen in **Figures 6A and 6B**, a new Fe(III)-dominant
37 mineral grain formed due to exposure to the fracture fluid that is larger than the neighboring

1 pyrite framboid. The fits of the four μ -XANES spectra collected for the Eagle Ford sample are
2 consistent with an array of Fe-bearing species. A fit of the μ -XANES spectra collected from the
3 pyrite grain seen in Spot 4 (**Figure 6A**) suggests preferential removal of sulfur from the pyrite as
4 indicated by the presence of pyrrhotite. Similar to the Marcellus samples, pyrite-rich zones in
5 the Eagle Ford samples also tend to contain magnetite. Unlike the Marcellus sample, however,
6 the Fe(III)-rich region seen in the Eagle Ford sample (**Figure 6B**) is dominated by hematite,
7 whereas the Marcellus samples contain ferrihydrite and goethite, but not hematite.

8 The Barnett shale showed the least amount of pyrite alteration and the lowest concentrations
9 of Fe(III)-bearing phases out of the four shale samples examined. The lack of significant Fe(III)-
10 bearing phases is consistent with the minimal buffering of the low-pH fracture fluid (**Figure 1**)
11 and little to no change in pyrite concentration shown by quantitative XRD (**Table 2**). Analysis of
12 the μ -XANES spectra indicates that the Fe(III)-bearing regions in the reacted shale are
13 comprised of magnetite, which may have been present in the rock before reaction, given that
14 Fe(III) in the form of magnetite is detected in unreacted shale and does not appear to have
15 been produced during the experiments (**Figure 3**).

16 The μ -XANES analysis of the Green River shale, following reaction, showed significant changes
17 in Fe speciation. A total of five Fe-rich regions were selected for collection of μ -XANES spectra.
18 Surprisingly, the five spectra collected were identical in shape. Differences among the μ -XANES
19 spectra collected for the samples reacted for 3-weeks, 3-months, and 6-months were minimal,
20 indicating little additional reaction of the Fe in the shale after three weeks. Because of the
21 higher sensitivity of EXAFS spectra than XANES spectra to Fe speciation, the bulk EXAFS spectra
22 of the reacted Green River shale are discussed below.

23 **Impact of Fracture Fluid on Speciation of Iron in Bulk Shale** - The bulk Fe K-edge EXAFS spectra
24 are complex, with pyrite being the dominant Fe-bearing phase for the Marcellus, Barnett, and
25 Eagle Ford shales we examined (**Table 4**). EXAFS analysis shows that the inorganic Fe species in
26 the unreacted sand-sized samples of Marcellus, Barnett, and Eagle Ford shales include pyrite,
27 goethite, ferrihydrite, and siderite (Eagle Ford only) (**Table 4**). As illustrated by the Marcellus
28 shale (**Figure 7**), the most notable difference common to the Fe K-edge EXAFS spectra of all four
29 shales samples is an additional oscillation in the spectra at $k = 3.6$ to 4.3 \AA^{-1} that is not found in
30 the Fe K-edge EXAFS spectrum of any of the 30 inorganic Fe(II)- and Fe(III)-bearing reference
31 compounds in our Fe XAS reference library. Because of this, shell-by-shell fitting of the spectra
32 was necessary to determine the potential backscatterer causing this oscillation in the EXAFS
33 spectra of the shale samples. The Fe K-edge EXAFS spectrum of an unreacted Marcellus shale
34 sample was selected for the initial shell-by-shell fitting because this extra oscillation is
35 particularly strong for the Marcellus shale. Over thirty FEFF-generated scattering pathways
36 were created between Fe(II) or Fe(III) and the ligands S, O, N, B, C, NO_3 , SO_3 , SO_4 , and CN at

1 distances reported for Fe organo-metallic molecules³⁶. The shell-by-shell fitting indicates that S
2 (organic), O, N, B, NO₃, SO₃, SO₄, and CN are not backscattering ligands around Fe in the
3 Marcellus shale sample. Instead, fitting of the EXAFS spectrum of the unreacted Marcellus
4 shale indicates that C is the most likely ligand around Fe, with an Fe(II)-C bond distance of 2.11
5 ± 0.02 Å. Thus, the Fe-C single scattering pathway is responsible for the unexplained EXAFS
6 oscillation at $k = 3.6$ to 4.3 \AA^{-1} . This distance is consistent with literature data where the vast
7 majority of Fe(II)-C bonds in organo-metallic molecules have bond distances between 2.06 and
8 2.14 Å³⁶. The Fe(II)-organic phase is most likely associated with the kerogen present in the
9 sample as blebs and ribbons dispersed throughout the shale (**Figure 8**). To get quantitative
10 estimates of the proportion of the Fe-C pair correlation relative to Fe-inorganic species pair
11 correlations in the shale samples, Fe-humate and ferrocene reference compounds were used in
12 the linear combination fitting of the XANES spectra. The shell-by-shell fitting of the EXAFS
13 spectra of the Fe-humate and ferrocene reference compounds shows that Fe is indeed bonded
14 to the C in both reference samples with Fe-C distances of $2.08 \pm 0.01 \text{ \AA}$ and $2.04 \pm 0.02 \text{ \AA}$,
15 respectively. Once the Fe-humate (denoted as Fe-organic) was included in the LCF, fitting of
16 the data improved significantly. In all unreacted and reacted shale samples, except for the
17 unreacted Eagle Ford shale sample, the Fe-organic phase is detectable. The Fe-organic phase
18 comprises between 12 and 33% of the total Fe species present in the shale samples (**Table 4**).

19 Similar to the results from μ -XANES analysis of the Green River shale, no pyrite was detected by
20 bulk EXAFS analysis of this shale. Unlike the other shale samples, a significant portion of the Fe
21 in the Green River shale is in the organic fraction. A shell-by-shell fit of the Fe K-edge EXAFS
22 spectrum of the 3-week-reacted Green River shale (**Figure 9**) shows that the Fe-C scattering
23 pathway makes a dominant contribution to the EXAFS spectrum, with an Fe-C distance of $2.13 \pm$
24 0.01 \AA . The full EXAFS spectrum was fit using the Fe-C scattering pathway, along with the Fe-S
25 (second-neighbor) and the Fe-Fe pathways from pyrite/pyrrhotite (**Figure 9**). The Fe-S first-
26 neighbor pathway makes a relatively minor contribution and is difficult to resolve due to the
27 very strong contribution of the Fe-C scattering pathway to the spectrum. Because of the
28 complexity of the Green River EXAFS spectrum and the high variability in local structure of Fe
29 bound to organic carbon, identifying the proper Fe-C organic reference compound for LCF
30 analysis is challenging. However, by using the Fe K-edge EXAFS spectrum for the unreacted
31 Green River shale and the spectrum for the 3-week reacted Green River kerogen isolated from
32 the same shale material, useful information can be derived from LCF analysis. The 3-week-
33 reacted Green River kerogen was selected for LCF because there is a detectable difference
34 between the unreacted and 3-week-reacted kerogen in the Fe EXAFS data with a slight shift of
35 the frequency of the EXAFS indicating a slightly shorter Fe-C bond distance (data not shown).
36 There is no detectable difference between the 3-week- and 3-month-reacted kerogen samples
37 (data not shown). By using the Fe K-edge EXAFS spectrum of the 3-week-reacted kerogen, a

1 more accurate fitting of the EXAFS spectrum of the 3-week-reacted shale could be
2 accomplished (**Table 4**). The best fit of the EXAFS spectrum of the 3-week-reacted Green River
3 shale is consistent with a combination of 55% of the unreacted shale and 45% of the 3-week-
4 reacted kerogen. The ratio of shale to kerogen decreased significantly for the 3-month-reacted
5 sample, with the unreacted shale component representing 40% and the isolated kerogen
6 comprising 60% of the spectrum. There is virtually no difference between the 3-month- and 6-
7 month-reacted samples.

8 **Bitumen/Fe Interactions** – The bitumens extracted from the Marcellus and Green River shales
9 are physically and chemically very different. The bitumen extracted from the Marcellus shale
10 was found to be mostly hydrophilic and readily dissolved into solution, whereas the Green River
11 bitumen has the consistency of hard tar and is very hydrophobic. Marcellus-derived bitumen
12 was the only bitumen that could be adequately dispersed into solution for dynamic light
13 scattering analysis. The Marcellus bitumen has a bi-modal distribution of particle sizes, with one
14 group of particles averaging 42 ± 3 nm in diameter and another group averaging 395 ± 15 nm in
15 diameter.

16 The simplified reactors containing only Fe(II), as FeCl_2 , and fracture fluid at pH = 2.0 (no
17 bitumen) had no detectable Fe(II) oxidation during a 6-week incubation. The amount of Fe(II)
18 oxidized was calculated by the loss of Fe(II) in solution compared with initial concentrations.
19 Reactors with added bitumen had significant Fe(II) oxidation over a 48 hour incubation time for
20 both pH 2.0 and 7.1 (**Figure 10**). The circum-neutral pH reactors with no fracture fluid showed
21 the greatest Fe(II) oxidation, with Green River and Marcellus bitumen having 41% and 28%,
22 respectively, of the Fe(II) oxidized to Fe(III) (**Figure 10**). The reactors containing fracture fluid,
23 including an Fe controlling agent (ethylene glycol), showed a slightly lower amount of oxidized
24 iron, with 25% oxidized for the Green River bitumen reactor and 23% oxidized for the Marcellus
25 bitumen reactor. Iron(II) oxidation did occur in the reactor containing only circum-neutral pH
26 fracture fluid (no bitumen), but the amount of oxidation was lower than in the bitumen-bearing
27 circum-neutral pH reactors. At low pH the addition of bitumen resulted in enhanced oxidation
28 of Fe in all reactors as well, but at lower amounts than at near-neutral pH, which is consistent
29 with known pH effects on aqueous iron oxidation³⁸. The presence of fracture fluid with
30 bitumen at low pH dramatically enhanced Fe oxidation in both the Green River bitumen
31 reactors (10% oxidized with no fracture fluid versus 20% oxidized with fracture fluid) and
32 Marcellus bitumen reactors (6.5% oxidized with no fracture fluid versus 21.0% oxidized with
33 fracture fluid) (**Figure 10**). XRD analysis of the Fe(III)-bearing precipitates indicates the
34 presence of 2-line ferrihydrite in all the reactors in which Fe(III) precipitation occurred after 48
35 hours of incubation. When the reactors were allowed to incubate for 3 weeks, the 2-line
36 ferrihydrite converted to goethite in reactors at pH = 2.0, whereas the 2-line ferrihydrite
37 converted to hematite in the reactors at pH = 7.1. Idealized reactors with the oxygen removed

1 from the system did not show any Fe(II) oxidation regardless of the pH and the presence or
2 absence of bitumen.

3 **Discussion:**

4 The reactivity of Fe-bearing species when exposed to fracture fluid varies significantly,
5 depending on the mineralogy of the host shale. The Fe μ -XRF maps coupled with μ -XANES
6 spectroscopy of the unreacted Barnett (2613 m depth), Marcellus (outcrop), Eagle Ford (3915
7 m depth), and Green River (outcrop) shales show that all samples exhibit common initial Fe
8 speciation with Fe-sulfide and magnetite dominating. Specifically Fe is dominantly present as
9 Fe(II) prior to reaction with the fracture fluid, and “hot spots” are dominated by pyrite or
10 pyrrhotite. The only detectable Fe(III)-bearing phase in hot spots was magnetite (**Figure 3**).
11 Notably, the only unreacted sample with detectable Fe(III)-(oxy)hydroxides (from bulk EXAFS
12 data) is the unreacted Barnett shale core collected from a depth of 2613 m (**Table 4**). Based on
13 direct measurements of Fe mineralogy and oxidation, the absence of oxidized Fe in unreacted
14 outcrop samples demonstrates that the outcrop samples considered here are not more
15 oxidized than core samples of Marcellus and Green River shales.

16 *Impact of Dissolved Oxygen on Iron Reactivity* - The presence of dissolved O₂ is necessary for
17 the oxidation of dissolved Fe in these shale systems. In reactors where O₂ was removed from
18 both the solution and headspace by sparging with Ar gas, none of the released Fe oxidized. The
19 use of oxygenated fluid for these reactors mirrors industrial hydraulic fracturing, where the
20 removal of dissolved O₂ from the injection fluids, either chemically or by sparging, is either
21 ineffective and/or not regularly performed. As a consequence, dissolved O₂ in fluids injected
22 into the subsurface is initially in equilibrium with atmospheric pO₂. Although there is a slight
23 chance that sample contamination occurred, Zolfaghari *et al.* (2016) showed that produced
24 waters from hydraulic fracturing of shales in Canada still contain dissolved O₂ at concentrations
25 near 9 mg/L²⁹. Even with significant quantities of dissolved O₂ in the shale reactors, the Fe that
26 is released from the shale, primarily from pyrite, is slow to oxidize due to the low pH of the
27 solution³⁸.

28 *Impact of pH on Fe Release and Oxidation Rates* - In the shale-hydraulic fracture fluid system,
29 HCl has the greatest influence on Fe release from shale. At the lower pH values of the Barnett
30 and Marcellus reactors (pH < 4.0), the rate of oxidation of released Fe(II) is expected to be ~3.2
31 orders of magnitude slower than at pH 7.0³⁸ (**Figure 11**). As a consequence of this slow
32 oxidation, Fe is present in solution for weeks to months (**Figure 2**). Under these conditions, Fe
33 can be transported away from point sources (pyrite, siderite, Fe-bearing clays, and Fe-bearing
34 phyllosilicates) prior to oxidizing and precipitating at other locations (**Figure 5**).

1 Fitting the bulk Fe K-edge EXAFS spectra of the Barnett and Marcellus shales resulted in an
2 unexpected conclusion. Because the fraction of the Fe-organic component based on the fits of
3 these spectra either does not change or increases with time, we conclude that Fe(II) associated
4 with the organic component (Fe-Kerogen) is the most stable form of Fe native to the shale and
5 that pyrite is the major source of Fe released during reaction of the shales with fracture fluid
6 (**Table 4**).

7 *Impact of Shale Mineralogy on Rates and Extent of Iron Oxidation-* Although O₂ controls the
8 oxidation and precipitation of Fe, it is reactive carbonate abundance that controls the
9 speciation and distribution of the Fe(III)-bearing precipitates. In oil/gas shales that have low
10 carbonate and thus low pH buffering capacities, such as the Marcellus and Barnett shale, the pH
11 values of the systems (at the solid:liquid ratios used in this study) remained low and did not rise
12 to circum-neutral levels (**Table 2 and Figure 1**). In these shales the slow oxidation of aqueous
13 Fe(II) produced highly dispersed Fe(III)-(oxy)hydroxide precipitates occurring at distances
14 greater than 50 μm from Fe(II)-bearing hot spots (**Figures 5A and 5B**).

15 We found large differences in the μ-XANES spectra at different locations within the reacted
16 Marcellus shale sample (**Figures 5A and 5B**) indicating significant variations in Fe speciation
17 (**Figure 5C**). The linear combination fits of the μ-XANES spectra show that the Fe(II) hot spots
18 (**Figure 5A**) are predominantly pyrite and magnetite, indicating partial oxidation of the pyrite
19 and resulting in a mixed Fe(II/III)-bearing particle being formed in place (**Figure 5D**). In regions
20 at a significant distance from the Fe(II) hot spots (> 20 μm), the Fe phases detected are
21 dominated by ferrihydrite and goethite (**Figures 5B and 5D**).

22 Eh/pH diagrams were constructed for the Marcellus reactors using Geochemist's Workbench³⁹
23 to understand the identity of the dominant Fe phases in the shale reactors at equilibrium. In a
24 situation where the Fe-controlling agents are working effectively, aqueous Fe(II) (either as a
25 hydrated ion or Fe-organic complex) should be the dominant form of Fe in solution over most
26 Eh and pH conditions in the subsurface (**Figure 12A**). However, when Fe-bearing minerals are
27 not suppressed in the thermodynamic modeling, hematite is the most stable Fe(III)-bearing
28 phase in these systems at equilibrium (**Figure 12B**). The relative scarceness of hematite in
29 reacted shales indicates that although hematite is thermodynamically favored, it is kinetically
30 limited in some of these systems. As seen in **Figure 12B**, as dissolved O₂ is consumed and Eh
31 decreases, Fe(II) becomes the predominant Fe species at equilibrium and further precipitation
32 of hematite should cease as long as new oxidants are not introduced to the system. Although
33 the emphasis for the low pH shale systems has been on the Marcellus shale, experimental
34 analyses of the Barnett shale produced similar results, with the exception that goethite, not
35 ferrihydrite, is the dominant Fe(III)-(oxy)hydroxide present (**Table 4**). When Fe(II) oxidizes and
36 precipitates in these systems with low pH buffering capacity, the Fe forms as diffuse Fe(III)-

1 (oxy)hydroxides that could coat not only fracture surfaces but also pore throats and piping used
2 in hydraulic fracturing operations.

3 It is surprising that at pH 3 to 4, Fe(II) oxidized and Fe(III)-bearing solids precipitated in the
4 Barnett and Marcellus reactors. The low pH of the system should retard oxidation of iron
5 compared to the circum-neutral conditions of the Eagle Ford and Green River reactors. One
6 possible reason for appreciable oxidation of Fe(II) under these conditions is the presence of
7 dissolved bitumen in solution.

8 Iron release and precipitate morphology, identity, and distribution differed significantly among
9 different shales at circum-neutral pH. For the carbonate-rich Eagle Ford and Green River
10 shales, little to no Fe was detectable in solution throughout the course of the 3-week, 3-month,
11 and 6-month incubation times, indicating that either no Fe was released from the shale or that
12 the Fe was released, oxidized, and precipitated as a solid too quickly to be detectable in
13 solution (**Figure 2**). The only experiments in which any Fe was detectable was in the Green
14 River reactor at 6 hours of incubation (**Figure 2**). Although the solution data do not indicate that
15 Fe(II) was released and oxidized to Fe(III), XRF mapping shows significantly more Fe(III) in the
16 reacted samples, indicating that Fe(II) was oxidized and precipitated in these carbonate-rich
17 shales. The close proximity of the Fe(III)-bearing phases (predominately hematite) near Fe
18 point sources, primarily pyrite framboids, indicates that released Fe does not travel far once
19 released, resulting in large mineral grains that could easily occlude nano- and micro-pores
20 (**Figure 6**). As seen in the Eagle Ford μ -XRF data (**Figure 6**), the Fe(III)-bearing particles, in this
21 case hematite, can be tens of microns in diameter. These results differ from poorly buffered,
22 low pH systems where Fe(III)-bearing precipitates were dispersed and of lower crystallinity than
23 those of the Eagle Ford and Green River shale systems. These large particles have the potential
24 to impact the porosity, permeability, and fluid movement near the Fe(II) sources, primarily
25 pyrite.

26 Although there are substantial differences between the low-carbonate and high-carbonate
27 shale-fracture fluid systems examined, there are some similarities. The first similarity is that O₂
28 is necessary for Fe(II) oxidation in the reactors for both types of system. The second is that in
29 all shales, inorganic Fe species (Fe-sulfides) were more reactive in the presence of fracture
30 fluids, compared to solutions lacking the fracture-fluid additives.

31 *Impact of Bitumen on Fe Oxidation Rates* - As **Figure 10** shows, the presence of bitumen can
32 override the retarding effect of low pH on the rates of Fe(II) oxidation. Jones *et al.*⁴⁰ showed
33 that in the presence of organics, molecular oxygen can oxidize Fe(II) at lower pH values and that
34 more complex organics, in particular EDTA and fulvic acid, further accelerated oxidation
35 compared to simpler organics, such as citric acid⁴⁰. Bitumen is classified based on three types of
36 organics: asphaltines + saturates, resins, and aromatics^{26, 27, 30, 31}. Although many chemicals are

1 used in dissolving bitumen, 2-ethyl hexanol, which is common to the fracture fluid formulations
2 used in this work, can readily extract bitumen from oil/gas shale²⁷. Thus, the release of bitumen
3 in hydraulically fractured subsurface systems can potentially play a significant role in pore
4 fouling and production loss, particularly in systems with low pH buffering capacity.

5 *Conceptual Model of Fe Behavior in Oil/Gas Shale*- A conceptual model that integrates these
6 results is presented in **Figure 13**. Iron precipitates, including both distribution and type of
7 phase, are highly dependent on the pH of the solution. Shales with high pH buffering capacity
8 (abundant carbonates) exhibit lower overall release of Fe(II). Because pH is maintained in the
9 near-neutral range, oxidation of released Fe(II) is relatively rapid, with the production of large
10 Fe(III)-(oxyhydr-)oxide grains or grain clusters (tens of microns in diameter) in proximity to the
11 original Fe(II) source, generally pyrite. These large particles will block porosity and inhibit gas
12 flow from the source rock to fracture space. Conversely, in shales where the pH stays low (shale
13 with low pH buffering capacity, or very close to the well bore), released Fe(II) is
14 thermodynamically more stable and is also slower to oxidize. Consequently, it can be
15 transported farther from the Fe source prior to oxidizing and/or precipitating (**Figure 13**). The
16 presence of abundant organics within the shale matrix that can be released by the organics in
17 fracture fluid is likely a key factor contributing to Fe(II) oxidation and subsequent Fe(III)-
18 (oxyhydr-)oxide precipitation at low pH. Although the sizes of these precipitates at lower pH
19 are smaller, they can precipitate farther from the source with the potential of occluding pores,
20 fractures, or wellbore piping far away from the source of Fe in the shale matrix. Our
21 experiments were designed to probe chemical reactions occurring within the first few hours or
22 days of fracture fluid-shale reaction, *i.e.*, during the time period when most of shale alteration
23 occurs and prior to unplugging of the well to allow escape of flowback. However, it is useful to
24 consider how high TDS, present in flowback, might affect our results. For example, recycled
25 flowback or produced water used for new hydraulic fractures is expected to have elevated TDS.
26 Because the reactors in our study used a higher fluid:solid mass ratio than occurs in the field,
27 the total dissolved solids (TDS) concentrations in these reactors are low relative to typical
28 values measured in flowback and produced waters (100's of g/L)⁴¹. As TDS increases to very
29 high concentrations (~200,000 ppm), the activity of Fe(II) and Fe(III) will decrease significantly
30 due to the formation of ion pairs (including iron-chloride pairs). However, given the high degree
31 of oversaturation in the reactors (calculated saturation indices >5), Fe(III)-(oxyhydr)oxide
32 precipitation is still likely to occur in the subsurface, though at potentially lower quantities and
33 slower rates. With regards to bitumen chemistry, based on the literature, high salinity should
34 have little to no impact on bitumen solubility²⁷. The type of organic solvent used in these
35 systems is the most important factor for bitumen extraction from the rock and is relatively
36 independent of salinity. Thus, although our studies provide fundamental insight into the
37 behavior of Fe(II) in shales exposed to hydraulic fracturing fluid, future studies examining the

1 role of high-TDS fluids would improve our ability to design procedures to improve production in
2 shale reservoirs.

3

4 **Implications:**

5 Oil/gas shales contain reduced Fe-bearing phases that release Fe(II) in the presence of acid and
6 O₂, which can subsequently be oxidized and result in the formation of Fe(III)-bearing
7 precipitates during hydraulic fracturing. In the four shale samples examined, Fe is associated
8 with a variety of phases: sulfides, clays, oxides, carbonates, and organics. Although there are
9 several potential sources that could release Fe into solution, EXAFS spectroscopy shows that
10 pyrite is more reactive with hydraulic fracture fluid than Fe(II) bound to organics. Reaction of
11 the shale samples with hydrochloric acid is necessary for the release of Fe into solution.
12 However, dissolved O₂ is critical for the oxidation of Fe(II) to Fe(III). At low pH, oxidation of
13 Fe(II) to Fe(III) is generally slow; however, we found that bitumen released from the shale by
14 the organics in fracture fluid reduces the inhibiting effect of hydrochloric acid on Fe(II)
15 oxidation and enhances oxidation at pH = 2.0. Thus bitumen in shale systems with low
16 buffering capacity (*i.e.* low concentrations of carbonate minerals) can play a major role in the
17 formation of Fe(III)-bearing precipitates that would otherwise not be expected to form. One
18 aspect that was not studied here is the potential impact of microorganisms in the subsurface on
19 the cycling of Fe. The dominant microbial groups present in the subsurface, in descending
20 order of abundance, are H₂S producers, anaerobic fermenters, and methanogens^{42, 43}. Because
21 of the high abundance of H₂S producers, there is the potential that a portion of the released
22 Fe(II) reacts with H₂S to precipitate Fe-sulfides (mackinawite) prior to oxidation. Although this
23 is a possibility, the impact is probably quite minor due to the presence of dissolved O₂ and
24 biocides injected into the subsurface that inhibit or kill H₂S-producing bacteria and the high
25 reactivity of mackinawite in the presence of O₂.

26 The importance of the pH buffering capacity of shales on the oxidation and precipitation of Fe-
27 bearing solids can not be overstated in the context of this study and is consistent with results of
28 a companion paper by Harrison *et al.* (*accepted*) as well as work by Wilke *et al.*⁴⁴. In systems
29 with low pH buffering capacity (*e.g.*, Marcellus and Barnett shales), released Fe(II) can stay in
30 solution for a significant amount of time, allowing diffusion and transport of Fe(II) to occur prior
31 to oxidation and precipitation of Fe(III)-bearing solids. When Fe(II) oxidation does occur in
32 carbonate-poor systems, the resultant Fe(III)-bearing precipitates are distributed in a diffuse
33 fashion and occur at significant distances from the Fe(II) point sources. These precipitates tend
34 to be comprised of ferrihydrite and goethite. The potential for transport of Fe released from
35 oil/gas shales can result in occlusion of pores, pore necks, and piping used in the hydraulic

1 fracturing process, which could (and most likely does) reduce production with time. In contrast,
2 in shales with high buffering capacity (Green River and Eagle Ford), released Fe(II) is quickly
3 oxidized and remains in close proximity to the point source.

4 **Conclusions:**

5 Our study of both well pH-buffered and poorly pH-buffered shale systems provides persuasive
6 evidence that oxidation and redistribution of Fe may play important roles in the rapid decrease
7 of hydrocarbon production with time that is observed in active wells following hydraulic
8 fracturing. Our study also shows that even though ethylene glycol (Fe-controlling agent)
9 injected into the subsurface can have an impact on Fe precipitation, this chemical appears to be
10 only partially effective in controlling Fe in solution. These findings indicate that additional
11 research on the types of chemicals injected, injection sequences, and the control of both acid
12 and dissolved O₂ is needed to control the behavior of Fe during hydraulic fracturing of oil/gas
13 shales. Such control could have the potential to increase both hydrocarbon production and the
14 efficiency of re-fracturing oil/gas shales, which could increase the utility of an already vital
15 portion of the energy portfolio of the United States.

16 **Acknowledgments:**

17 We would like to thank Dr. Arjun Kholi of Stanford University for providing the Eagle Ford and
18 Barnett shale samples used in this work. We would also like to thank Drs. Sam Webb and
19 Courtney Roach (SSRL) for helping with XRF and μ -XANES data collection on beamline 2-3 and
20 Ryan Davis (SSRL) for assistance in collecting the Fe bulk EXAFS data on beamline 4-1.
21 Additional thanks go to Drs. Vincent Noel and Naresh Kumar of Stanford University plus Dr.
22 Jason Stuckey of University of Delaware for providing Fe EXAFS reference spectra used in fitting
23 of the x-ray absorption spectra in this study. We would also like to thank the staff of the
24 Stanford Nano Shared Facility for help with SEM imaging. We gratefully acknowledge the
25 funding for this project provided via a grant by the National Energy Technology Laboratory to
26 SLAC under Contract #DE-AC02-765F00515.

1 **Literature Cited:**

- 2 1. Wang, Z.; Krupnick, A. *A Retrospective Review of Shale Gas Development in the United States;*
3 Resources for the Future: Washington D.C., 2013; p 42.
- 4 2. Zhang, P.; Hu, L.; Meegoda, J. N.; Gao, S., Micro/Nano-pore Network Analysis of Gas flow in
5 Shale Matrix. *Nature Scientific Reports* **2015**, 5, 1-11.
- 6 3. Bustin, A. M. M.; Bustin, R. M., Importance of rock properties on the producibility of gas shales.
7 *International Journal of Coal Geology* **2012**, 103, 132-147.
- 8 4. Patzek, T. W.; Male, F.; Marder, M., Gas production in the Barnett Shale obeys a simple scaling
9 theory. *Proceedings of the National Academy of Science* **2013**, 110, (49), 19731-19736.
- 10 5. Monteiro, P. J. M.; Rycroft, C. H.; Barenblatt, G. I., A Mathematical Model of Fluid and Gas Flow
11 in Nanoporous Media. *Proceedings of the National Academy of Science* **2013**, 109, (50), 20309-
12 20313.
- 13 6. Liu, J.; Wang, J. G.; Gao, F.; Ju, Y.; Zhang, X.; Zhang, L.-C., Flow Consistency Between Non-Darcy
14 Flow in Fracture Network and Nonlinear Diffusion in Matrix to Gas Production Rate in Fractured
15 Shale Gas Reservoirs. *Transport in Porous Media* **2016**, 111, 97-121.
- 16 7. Falk, K.; Coasne, B.; Pellenq, R.; Ulm, F.-J.; Bocquet, L., Subcontinuum Mass Transport of
17 Condensed Hydrocarbons in Nanoporous Media. *Nature Communications* **2015**, 6, 1-7.
- 18 8. Karra, S.; Makedonska, N.; Viswanathan, H. S.; Painter, S. L.; Hyman, J. D., Effect of Advective
19 Flow in Fractures and Matrix Diffusion on Natural Gas Production. *Water Resources Research*
20 **2015**, 51, 8646-8657.
- 21 9. Chermak, J. A.; Schreiber, M. E., Mineralogy and Trace Element Geochemistry of Gas Shales in
22 the United States: Environmental Implications. *International Journal of Coal Geology* **2014**, 126,
23 32-44.
- 24 10. Ground Water Protection Council; Interstate Oil & Gas Compact Commission. FracFocus
25 Chemical Disclosure Registry. **2016**.
- 26 11. Abualfaraj, N.; Gurian, P. L.; Olson, M. S., Characterization of Marcellus Shale Flowback Water.
27 *Environmental Engineering Science* **2014**, 31, (9), 514-524.
- 28 12. Balashov, V. N.; Engelder, T.; Gu, X.; Fantle, M. S.; Brantley, S. L., A Model Describing Flowback
29 Chemistry Changes with Time After Marcellus Shale Hydraulic Fracturing. *AAPG Bulletin* **2015**,
30 99, (1), 143-154.
- 31 13. Ghanbari, E.; Dehghanpour, H., The Fate of Fracturing Water: A Field and Simulation Study. *Fuel*
32 **2016**, 163, 282-294.
- 33 14. Lester, Y.; Ferrer, I.; Thurman, E. M.; Sitterley, K.; Korak, J. A.; Aiken, G.; Linden, K. G.,
34 Characterization of Hydraulic Fracturing flowback Water in Colorado: Implications for Water
35 Treatment. *Science of the Total Environment* **2015**, 512-513, 637-644.
- 36 15. Munirasu, S.; Haija, M. A.; Banat, F., Use of Membrane Technology for Oil Field and Refinery
37 Produced Water Treatment-A Review. *Process Safety and Environmental Protection* **2016**, 100,
38 183-202.
- 39 16. Vikram, A.; Lipus, D.; Bibby, K., Produced Water Exposure Alters Bacterial Response to Biocides.
40 *Environmental Science & Technology* **2014**, 48, 13001-13009.
- 41 17. Wang, L.; Fortner, J. D.; Giammar, D. E., Impact of Water Chemistry on Element Mobilization
42 from Eagle Ford Shale. *Environmental Engineering Science* **2015**, 32, (4), 310-320.
- 43 18. Chalmers, G. R.; Bustin, R. M.; Power, I. M., Characterization of Gas Shale Pore Systems by
44 Porosimetry, Pycnometry, Surface Area, and Field Emission Scanning Electron
45 Microscopy/Transmission Electron Microscopy Image Analyses: Examples from the Barnett,
46 Woodford, Haynesville, Marcellus, and Doig Units. *AAPG Bulletin* **2012**, 96, (6), 1099-1119.

- 1 19. Curtis, M. E.; Sondergeld, C. H.; Ambrose, R. J.; Rai, C. S., Microstructural Investigation of Gas
2 Shales in Two and Three Dimensions Using Nanometer-scale Resolution Imaging. *AAPG Bulletin*
3 **2012**, 96, (4), 665-677.
- 4 20. Davies, R. J.; Mathias, S. A.; Moss, J.; Hustoft, S.; Newport, L., Hydraulic Fractures: How Far Can
5 They Go? *Marine and Petroleum Geology* **2012**, 37, 1-6.
- 6 21. Gale, J. F. W.; Laubach, S. E.; Olson, J. E.; Eichhubl, P.; Fall, A., Natural Fractures in Shale: A
7 Review and New Observations. *AAPG Bulletin* **2014**, 98, (11), 2165-2216.
- 8 22. Gale, J. F. W.; Reed, R. M.; Holder, J., Natural Fractures in the Barnett Shale and Their
9 Importance for Hydraulic Fracture Treatments. *AAPG Bulletin* **2007**, 91, (4), 603-622.
- 10 23. Hammack, R. W.; Harbert, W.; Sharma, S.; Stewart, B. W.; Capo, R. C.; Wall, A. J.; Wells, A.; Diehl,
11 R.; Blaushild, D.; Sams, J.; Veloski, G. *An Evaluation of Fracture Growth and Gas/Fluid Migration*
12 *as Horizontal Marcellus Shale Gas Wells are Hydraulically Fractured in Greene County,*
13 *Pennsylvania*; National Energy Technology Laboratory: Pittsburgh, 2014; p 76.
- 14 24. Harris, W. M.; Chiu, W. K. S., Determining the Representative Volume Element Size for Three-
15 dimensional Microstructural Material Characterization. Part 1: Predictive Models. *Journal of*
16 *Power Sources* **2015**, 282, 552-561.
- 17 25. Milliken, K. L.; Rudnicki, M.; Awwiller, D. N.; Zhang, T., Organic Matter-hosted Pore System,
18 Marcellus Formation (Devonian), Pennsylvania. *AAPG Bulletin* **2013**, 97, (2), 177-200.
- 19 26. Loeber, L.; Muller, G.; Morel, J.; Sutton, O., Bitumen in Colloid Science: A Chemical, Structural
20 and Rheological Approach. *Fuel* **1998**, 77, (13), 1443-1450.
- 21 27. Redelius, P. G., Solubility Parameters and Bitumen. *Fuel* **2000**, 79, 27-35.
- 22 28. Goklen, K. E.; Stoecker, T. J.; Baddour, R. F., A Method for the Isolation of Kerogen from Green
23 River Oil Shale. *Industrial & Engineering Chemistry Product Research and Development* **1984**, 23,
24 308-311.
- 25 29. Zolfaghari, A.; Dehghanpour, H.; Noel, M.; Beringer, D., Laboratory and Field Analysis of
26 Flowback Water from Gas Shales. *Journal of Unconventional Oil and Gas Resources* **2016**, 14,
27 113-127.
- 28 30. Redelius, P.; Soenen, H., Relation Between Bitumen Chemistry and Performance. *Fuel* **2015**, 140,
29 34-43.
- 30 31. Traxler, R. N., The Physical Chemistry of Asphaltic Bitumen. *Chemical Reviews* **1936**, 19, (2), 119-
31 143.
- 32 32. Materials Data, Inc. *Jade XRD Pattern Processing Ver. 6.5*, **2002**.
- 33 33. Webb, S. *SMAK: Sam's Microprobe Analysis Kit Ver. 0.50*, **2006**.
- 34 34. Webb, S. *SixPACK*, 0.63; Stanford Synchrotron Radiation Laboratory: Menlo Park, **2006**.
- 35 35. Webb, S. M., SIXPack: a graphical user interface for XAS analysis using IFEFFIT. *Physica Scripta*
36 **2005**, T115, 1011-1014.
- 37 36. Kruger, C.; Barnett, B. L.; Brauer, D., *The Organic Chemistry of Iron: Volume I*. Academic Press:
38 New York, **1978**; p 672.
- 39 37. Ankudinov, A. L.; Ravel, B.; Rehr, J. J.; Conradson, S. D., Real-space Multiple-scattering
40 Calculation and Interpretation of X-ray Absorption Near-edge Structure. *Physica Review B* **1998**,
41 58, (12), 7565-7576.
- 42 38. Morgan, B.; Lahav, O., The effect of pH on the kinetics of spontaneous Fe(II) oxidation by O₂ in
43 aqueous solution - basic principles a simple heuristic description. *Chemosphere* **2007**, 68, (11),
44 2080-2084.
- 45 39. *The Geochemist's Workbench 8.0*; Aqueous Solutions, LLC: **2009**.
- 46 40. Jones, A. M.; Griffin, P. J.; Waite, T. D., Ferrous Iron Oxidation by Molecular Oxygen Under Acidic
47 Conditions: The Effect of Citrate, EDTA and Fulvic Acid. *Geochimica et Cosmochimica Acta* **2015**,
48 160, 117-131.

1 41. Haluszczak, L. O.; Rose, A. W.; Kump, L. R., Geochemical evaluation of flowback brine from
2 Marcellus gas wells in Pennsylvania, USA. *Applied Geochemistry* **2013**, 28, 55-61.

3 42. Cluff, M. A.; Hartsock, A.; MacRae, J. D.; Carter, K.; Mouser, P. J., Temporal Changes in Microbial
4 Ecology and Geochemistry in Produced Water from Hydraulically Fractured Marcellus Shale Gas
5 Wells. *Environmental Science & Technology* **2014**, 48, 6508-6517.

6 43. Akob, D. M.; Cozzarelli, I. M.; Dunlap, D. S.; Rowan, E. L.; Lorah, M. M., Organic and Inorganic
7 Composition and Microbiology of Produced Waters from Pennsylvania Shale Gas Wells. *Applied*
8 *Geochemistry* **2015**, 60, 116-125.

9 44. Wilke, F. D. H.; Vieth-Hillebrand, A.; Naumann, R.; Erzinger, J.; Horsfield, B., Induced Mobility of
10 Inorganic and Organic Solutes from Black Shales using Water Extraction: Implications for Shale
11 Gas Exploitation. *Applied Geochemistry* **2015**, 63, 158-168.

12 45. McKibben, M. A.; Barnes, H. L., Oxidation of pyrite in low temperature acidic solutions: Rate
13 laws and surface textures. *Geochimica et Cosmochimica Acta* **1986**, 50, 1509-1520.

14
15
16

Ingredient	Purpose	By Mass	Percentage of Ingredient (wt.%)
Water	Base Fluid	1995.6674 g	99.783%
Ethylene Glycol	Scale Inhibitor, Iron Control, Breaker	0.4113 g	0.021%
Kerosene	Friction Reducer	0.4815 g	0.024%
Guar Gum	Dry Gellant	0.5807 g	0.029%
2-Ethyl hexanol	Corrosion Inhibitor for Acid	0.0093 g	0.0005%
Glycol ether	Corrosion Inhibitor for Acid	0.0031 g	0.0002%
Polyethylene glycol	Biocide	0.3974 g	0.020%
Hydrochloric acid	Acid	2.4493 g	0.122%

1
2
3
4
5
6
7
8
9
10
11
12
13
14
15
16
17
18
19
20

Table 1: Fracture-fluid composition used in experiments based on reported additives used at Marcellus Shale gas Well E. Silica Proppant and two biocides (2,2-Dibromo-3-nitrilopropionamide and Dibromoacetonitrile) were removed from the formulation. Polyethylene glycol represents more than 60% of the total biocide introduced into Well E. Solution pH = 2.00

Sample	Quartz	Calcite	Dolomite	Illite	Kaolinite	Pyrite	Feldspar	Analcime
Barnett Initial	44.2	8.2	X	40.6	X	2.1	4.9	X
Barnett 3 Week	68.4	X	X	29.1	X	2.5	X	X
Barnett 3 Week Dup	65.9	X	X	31.9	X	2.2	X	X
Barnett 3 Month	68.2	X	X	29.0	X	2.8	X	X
Barnett 6 Month	64.1	X	X	33.8	X	2.1	X	X
Marcellus Initial	42.2	11.6	1.1	35.0	X	6.4	3.7	X
Marcellus 3 Week	66.0	X	X	28.1	X	5.9	X	X
Marcellus 3 Month	60.6	X	X	34.3	X	5.1	X	X
Marcellus 3 Month Dup	61.3	X	X	33.4	X	5.3	X	X
Marcellus 6 Month	52.0	X	X	43.8	X	4.2	X	X
Marcellus 3 Week No O ₂	59.7	X	X	34.9	X	5.4	X	X
Eagle Ford Initial	25.2	64.5	X	X	7.6	2.7	X	X
Eagle Ford 3 Week	34.3	54.0	X	X	7.7	4.0	X	X
Eagle Ford 3 Month	36.4	52.5	X	X	7.3	3.8	X	X
Eagle Ford 6 Month	36.5	52.8	X	X	7.9	2.8	X	X
Green River Initial	31.4	23.2	28.9	X	X	X	8.0	8.5
Green River 3 Week	23.3	17.7	41.9	9.2	X	X	4.3	3.6
Green River 3 Month	23.3	20.2	36.9	11.2	X	X	5.3	3.1
Green River 6 Month	23.4	19.3	40.3	9.5	X	X	4.3	3.2

1 **Table 2:** Quantitative XRD results of sand-sized oil/gas shale samples. Quantitative results are derived
2 from least-squares fitting of the data using the JADE diffraction software. All values are in wt.% with "X"
3 denoting a non-detect for the phase. Uncertainty for fits to phases is $\leq 15\%$, detection limit is 0.1 wt.%.

4

1

Sample	Na (wt.%)	K (wt.%)	Ca (wt.%)	Mg (wt.%)	Al (wt.%)	Si (wt.%)	Fe (mg/g)	TC (wt.%)
Barnett Initial	0.103	1.646	2.509	0.631	7.291	25.53	24.83	16.00
Barnett 3 Week	0.115	1.882	0.136	0.348	7.674	28.64	20.79	4.29
Barnett 3 Week Dup	0.089	1.811	0.090	0.486	10.28	34.52	20.51	4.44
Barnett 3 Month	< 0.01	1.763	0.064	0.321	7.081	25.86	18.99	4.56
Barnett 6 Month	< 0.01	1.447	0.054	0.457	10.81	34.91	15.36	4.60
Marcellus Initial	< 0.01	2.069	4.227	0.784	10.5	28.41	45.63	6.04
Marcellus 3 Week	< 0.01	1.872	2.781	0.589	6.535	21.04	36.88	5.86
Marcellus 3 Month	< 0.01	2.098	0.073	0.792	11.02	31.97	30.38	5.77
Marcellus 3 Month Dup	< 0.01	2.105	0.151	0.498	7.17	23.78	32.55	5.76
Marcellus 6 Month	< 0.01	2.328	0.251	0.574	8.003	26.20	37.60	6.05
Marcellus 3 Week No O ₂	< 0.01	3.023	0.019	0.719	8.757	25.16	40.96	6.18
Eagle Ford Initial	< 0.01	0.886	16.67	0.371	5.818	15.97	21.17	4.42
Eagle Ford 3 Week	< 0.01	0.979	13.46	0.468	6.376	17.93	23.93	9.90
Eagle Ford 3 Month	< 0.01	1.025	12.87	0.469	6.232	18.14	22.45	8.84
Eagle Ford 6 Month	< 0.01	0.882	10.49	0.412	5.306	15.42	19.26	9.99
Green River Initial	0.943	1.074	13.64	4.414	2.662	12.27	17.83	12.71
Green River 3 Week	1.012	1.399	13.08	4.43	3.632	15.97	22.15	13.44
Green River 3 Month	0.874	1.184	9.108	3.696	2.76	17.93	13.61	12.29
Green River 6 Month	0.856	1.121	10.23	3.50	2.991	12.85	17.50	11.99

2

3 **Table 3:** Bulk XRF measurements of selected elements for sand-sized oil/gas shale samples. Uncertainty
4 for triplicate measurements is $\leq 5\%$, 1 SD. Total Carbon (TC) was analyzed using Dumas combustion.

5

6

Barnett Sample	Pyrite	Goethite	Fe-Organics	Residual			
Initial	0.67	0.21	0.12	0.721			
3 Week	0.72	0.12	0.16	0.758			
3 Week Duplicate	0.69	0.15	0.16	0.772			
3 Month	0.75	0.11	0.14	0.938			
6 Month	0.69	0.13	0.18	0.681			
Marcellus Sample	Pyrite	Ferrihydrite	Hornblende	Biotite	Fe-Organics	Residual	
Initial	0.53	X	0.08	0.26	0.13	0.840	
3 Week	0.64	0.16	X	X	0.20	0.915	
3 Month	0.65	0.20	X	X	0.15	0.874	
3 Month Duplicate	0.64	0.18	X	X	0.18	0.965	
6 Month	0.62	0.11	X	X	0.27	0.529	
Eagle Ford Sample	Pyrite	Ferrihydrite	Goethite	Hematite	Siderite	Fe-Organics	Residual
Initial	0.92	X	X	X	0.08	X	0.987
3 Week	0.61	X	0.20	X	X	0.19	0.752
3 Month	0.65	X	0.18	X	X	0.17	0.862
6 Month	0.47	X	X	0.20	X	0.33	0.793
Green River Sample	GR Initial Shale	GR 3 Week Reacted Shale	GR 3 Week Reacted Kerogen	Residual			
3 Week	0.55		0.45	0.706			
3 Month		0.40	0.60	0.320			
6 Month		0.40	0.60	0.264			

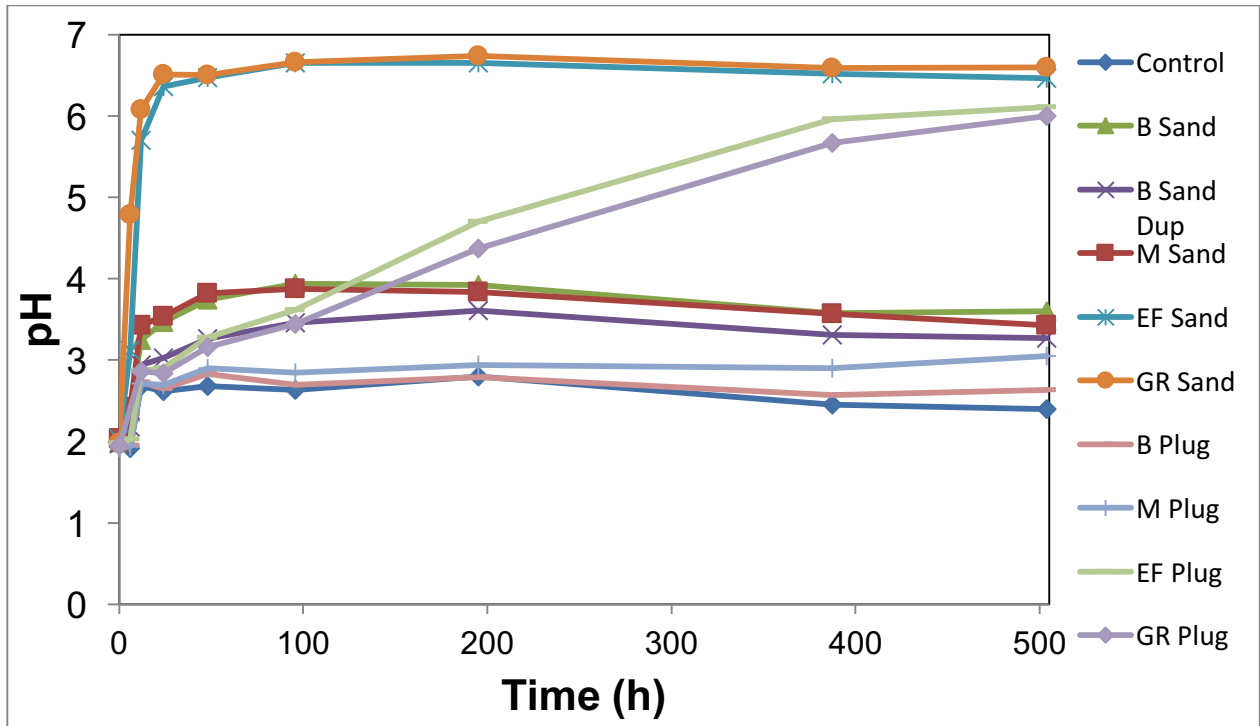
1

2 **Table 4:** Results of linear combination fitting of the bulk Fe K-edge EXAFS for sand-sized oil/gas shale
3 samples. The Fe-C component was fit using an Fe-humate reference spectrum. Uncertainty for all
4 fitting components is $\leq 10\%$, 1 SD. Non-detects are denoted as X.

5

6

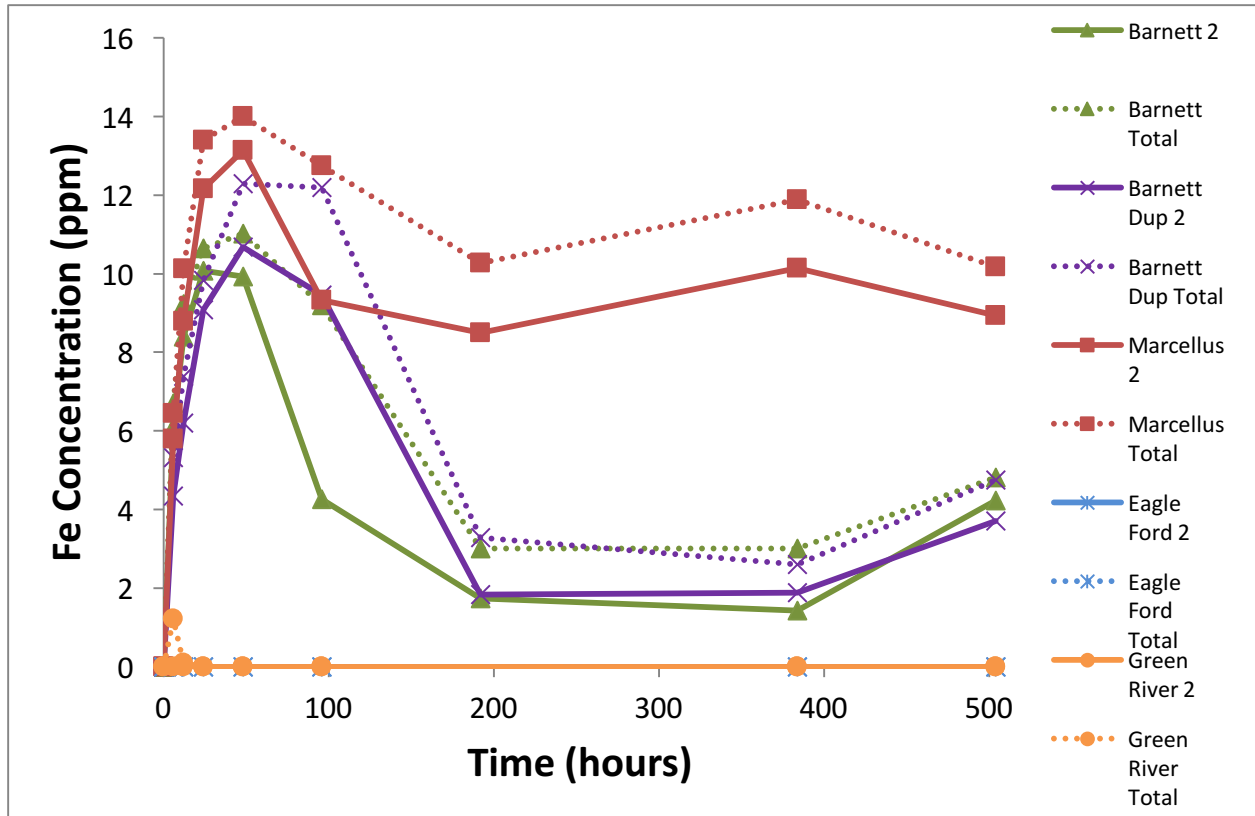
7



1
2
3
4
5
6
7

Figure 1: pH measurements of 3 week reactors for all four shale samples. M = Marcellus, B = Barnett, EF = Eagle Ford, and GR = Green River. Control contains all fracture fluid components but no shale material. Plug, refers to whole shale pieces that are not ground. Uncertainty in triplicate measurements is less than 0.05 pH units.

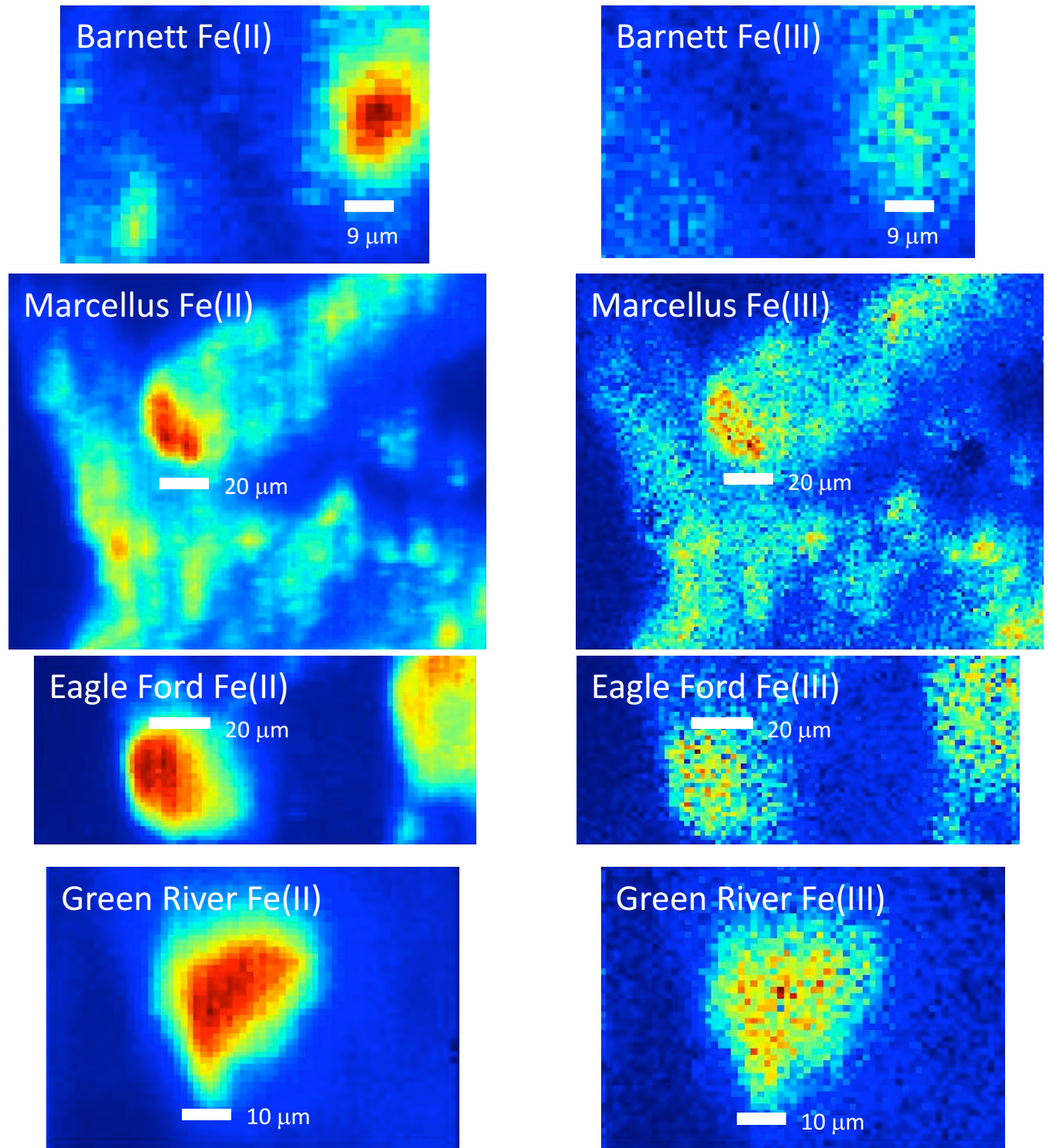
1



2

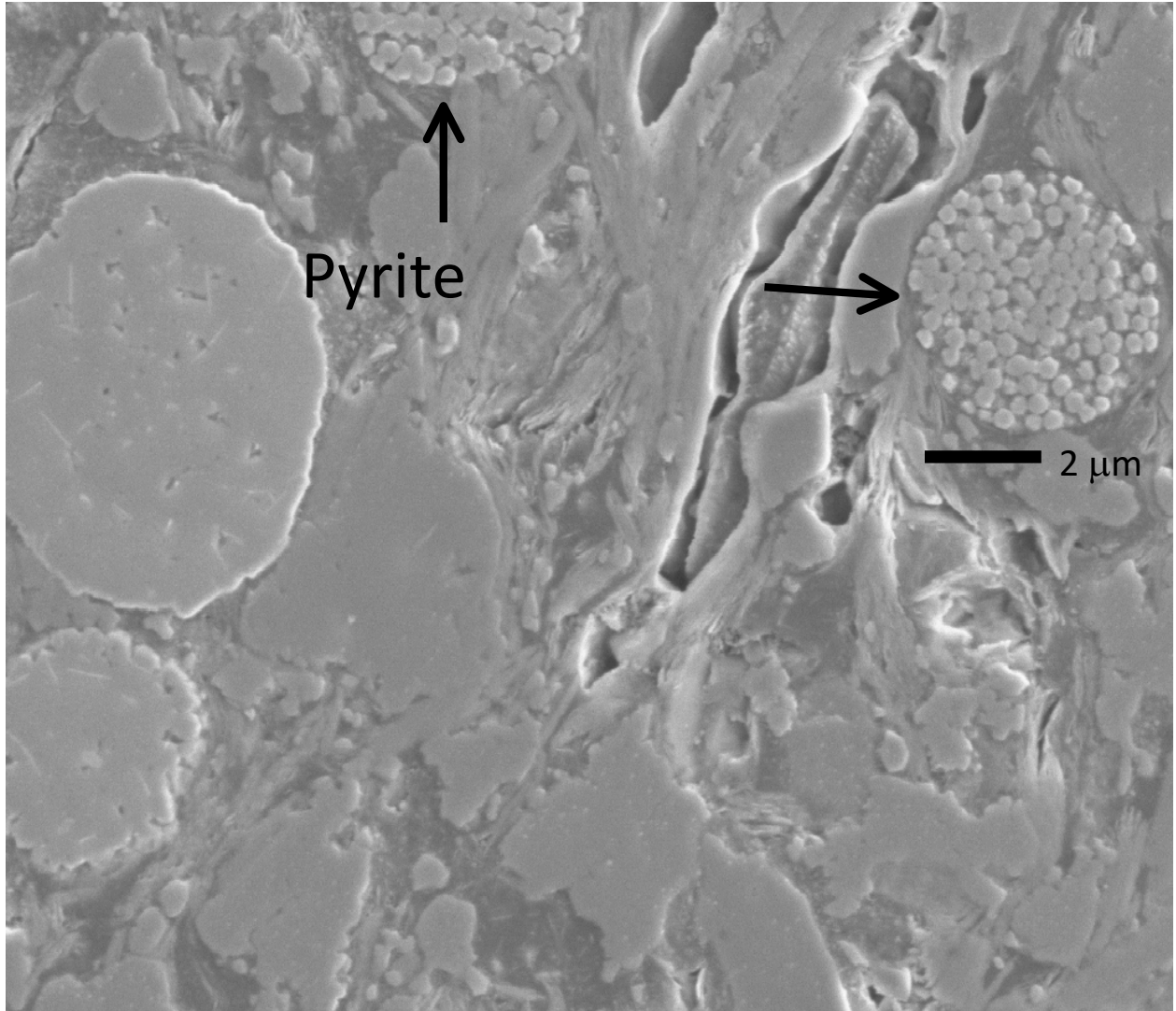
3 **Figure 2:** Iron release curve from sand-sized shale samples. The number "2" denotes Fe(II)
4 concentrations while "Total" denotes total Fe concentrations in solution. Uncertainty in triplicate
5 samples is < 8%.

6



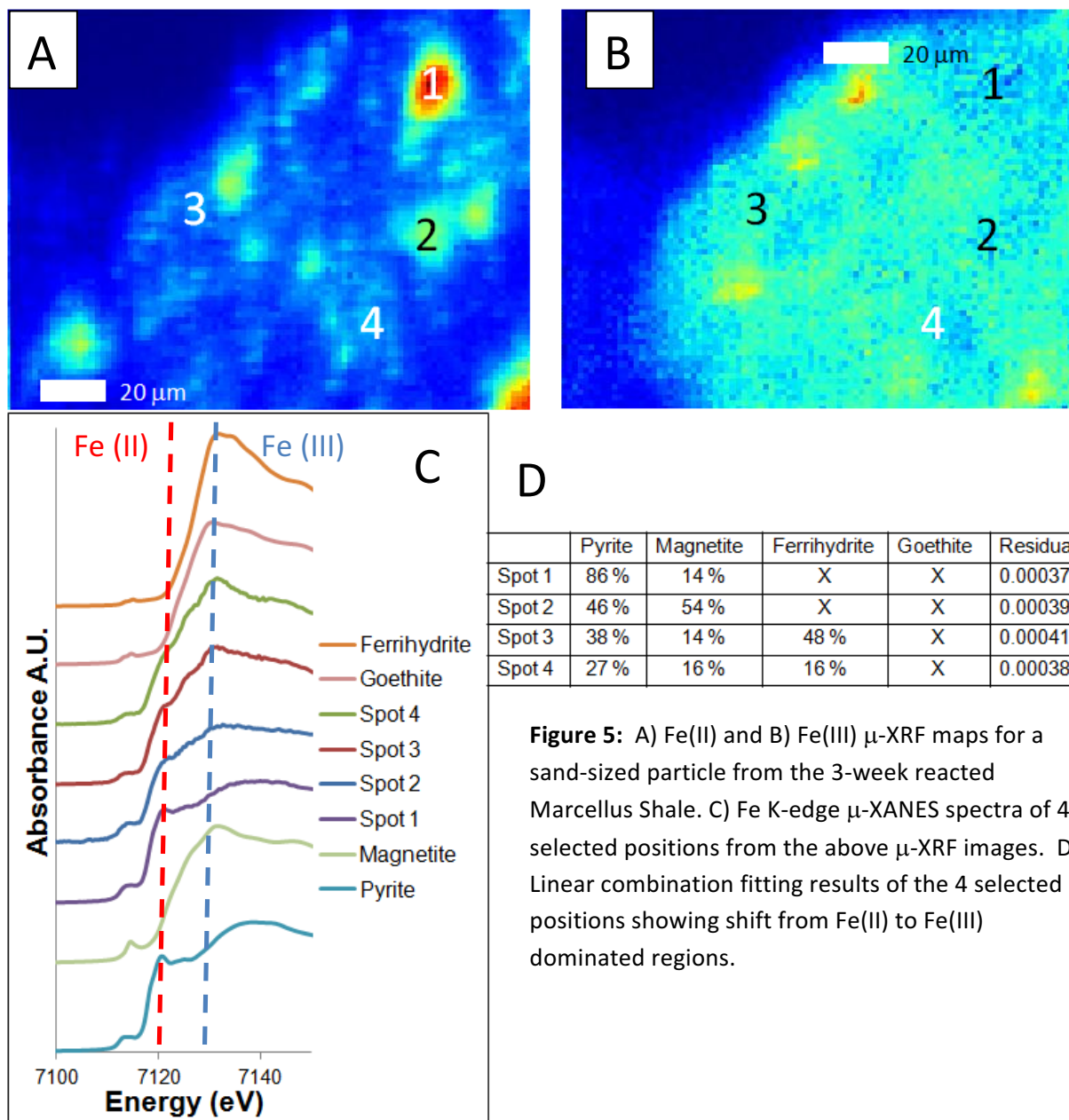
1
 2 **Figure 3:** Iron K-edge synchrotron μ -XRF imaging of the initial oil/gas shale sand-sized samples. Pyrite is
 3 the dominant Fe(II)-bearing phase for Barnett, Eagle Ford, and Marcellus with Fe(III) rich regions being
 4 almost exclusively magnetite. Pyrrhotite is the primary Fe(II)-bearing phase for Green River with
 5 magnetite being the primary Fe(III)-bearing phase.

1



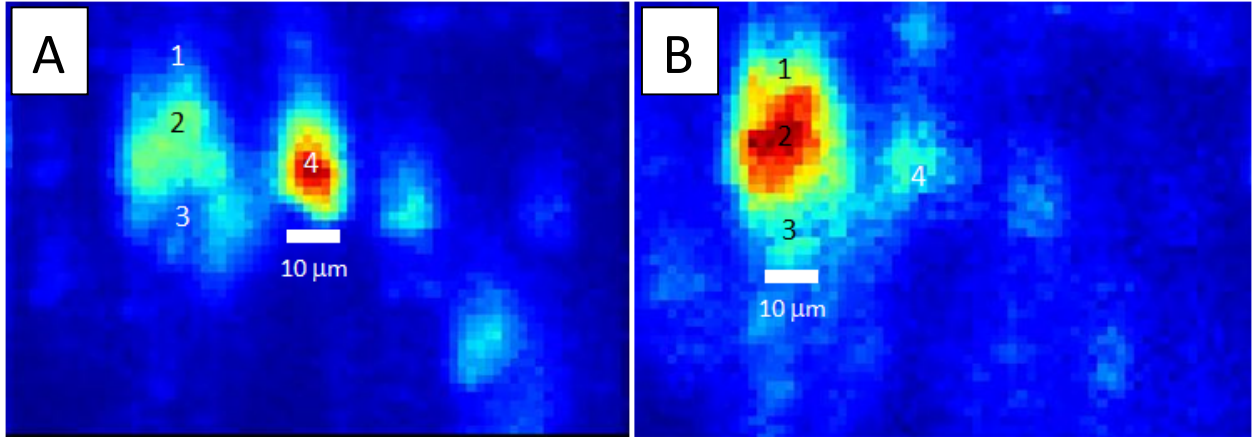
2

3 **Figure 4:** Scanning electron microscope image of unreacted Marcellus shale showing framboidal pyrites;
4 image collected from sand-sized shale sample.



1

2



1

	Pyrite	Pyrrhotite	Magnetite	Hematite	Residual
Spot 1	19 %	X	37 %	45 %	0.002858
Spot 2	12 %	X	37 %	51 %	0.003642
Spot 3	41 %	X	36 %	23 %	0.000165
Spot 4	54 %	34 %	12 %	X	0.000677

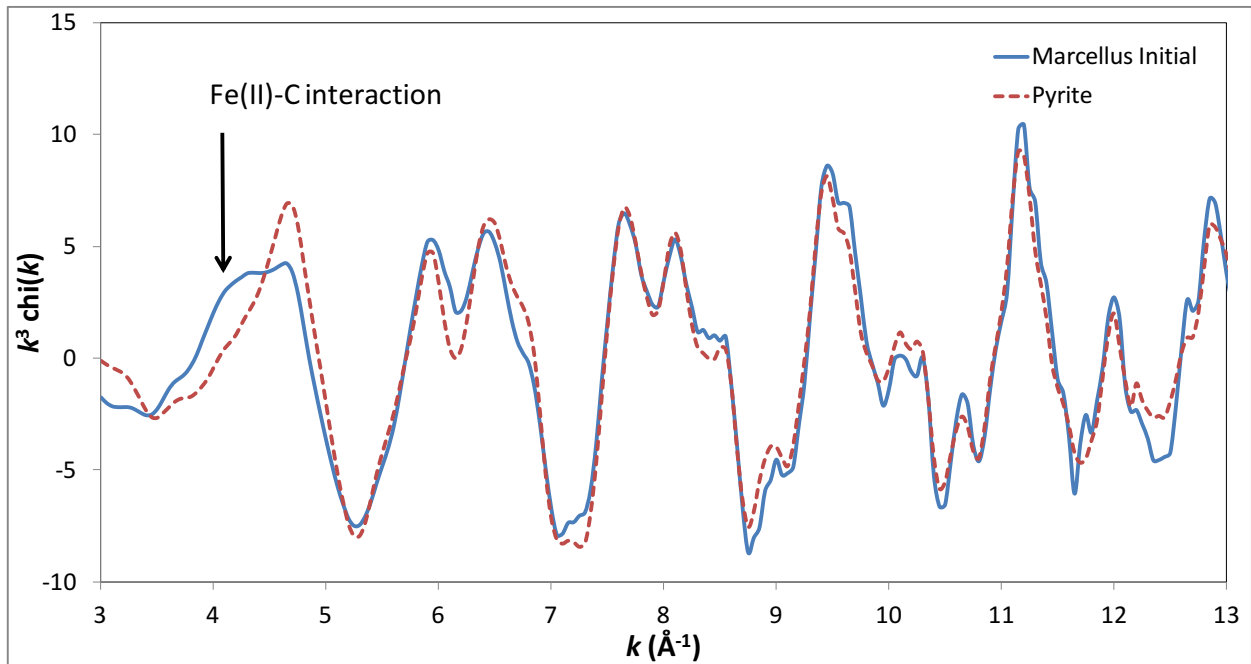
2

3 **Figure 6:** A) Fe(II) and B) Fe(III) μ -XRF maps for a sand-sized particle from the 3-week reacted Eagle Ford
 4 Shale. C) Linear combination fitting results of the 4 selected positions showing shift from Fe(II) to Fe(III)
 5 dominated regions with the presence of significant quantities of hematite. Non-detects are denoted as
 6 "X".

7

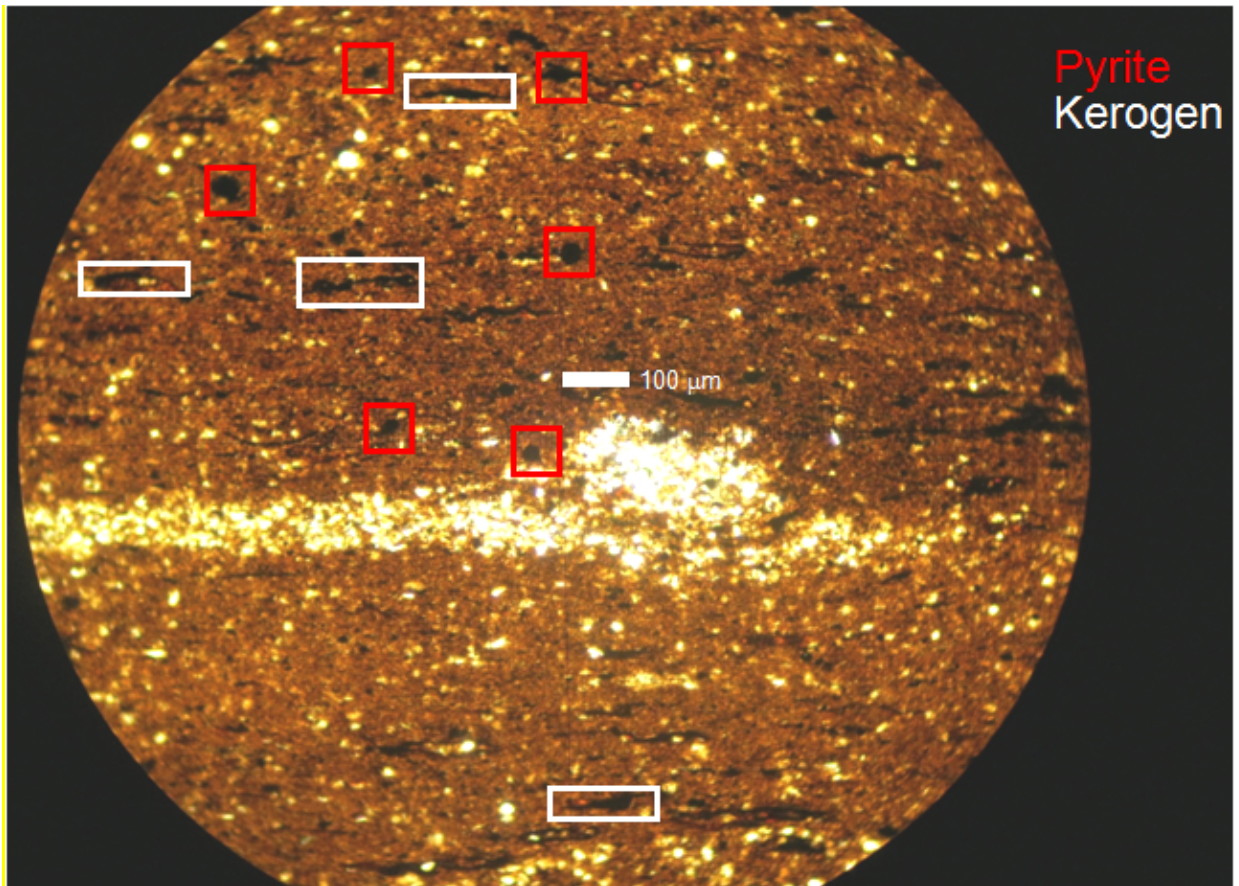
8

9



1

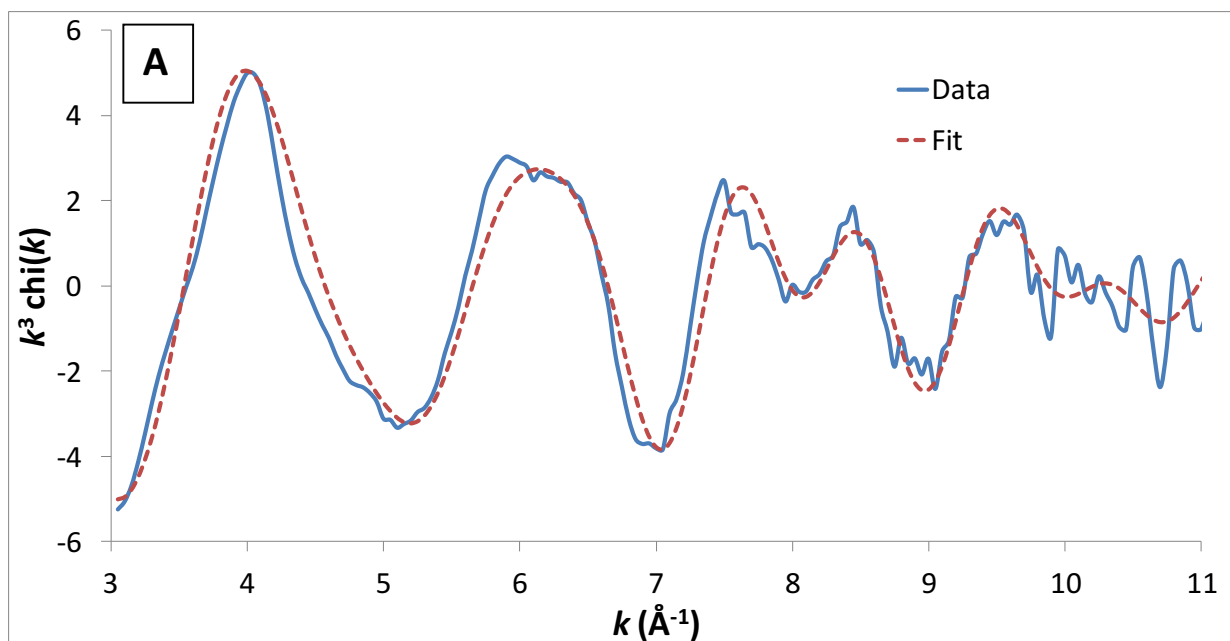
2 **Figure 7:** Bulk Fe K-edge EXAFS of the Marcellus shale prior to reaction with hydraulic fracturing fluid.
 3 The dashed line is a pyrite reference compound illustrating that the majority of the features are due to
 4 pyrite. The feature at $k = 4$ is not consistent with any inorganic Fe compound in the reference library.
 5 Shell-by-shell fitting of the data indicates that the feature at $k = 4$ is consistent with an Fe(II)/C
 6 interaction at 2.11 Å.



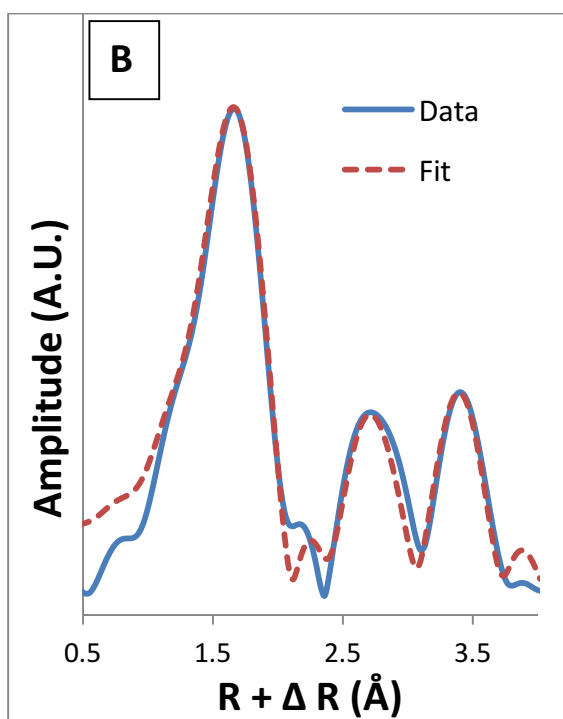
1

2 **Figure 8:** Petrographic thin section cut from a large piece of Marcellus shale (original block was 20 cm x
3 20 cm x 10 cm) under plain polarized light, thin section was cut perpendicular to bedding. The white
4 boxes illustrates the typical morphology and high abundance of kerogen in the shale while the red boxes
5 indicates typical morphology of pyrite. White minerals in the thin section are quartz crystals while the
6 brown colored matrix material is mostly clay minerals.

7



1



2

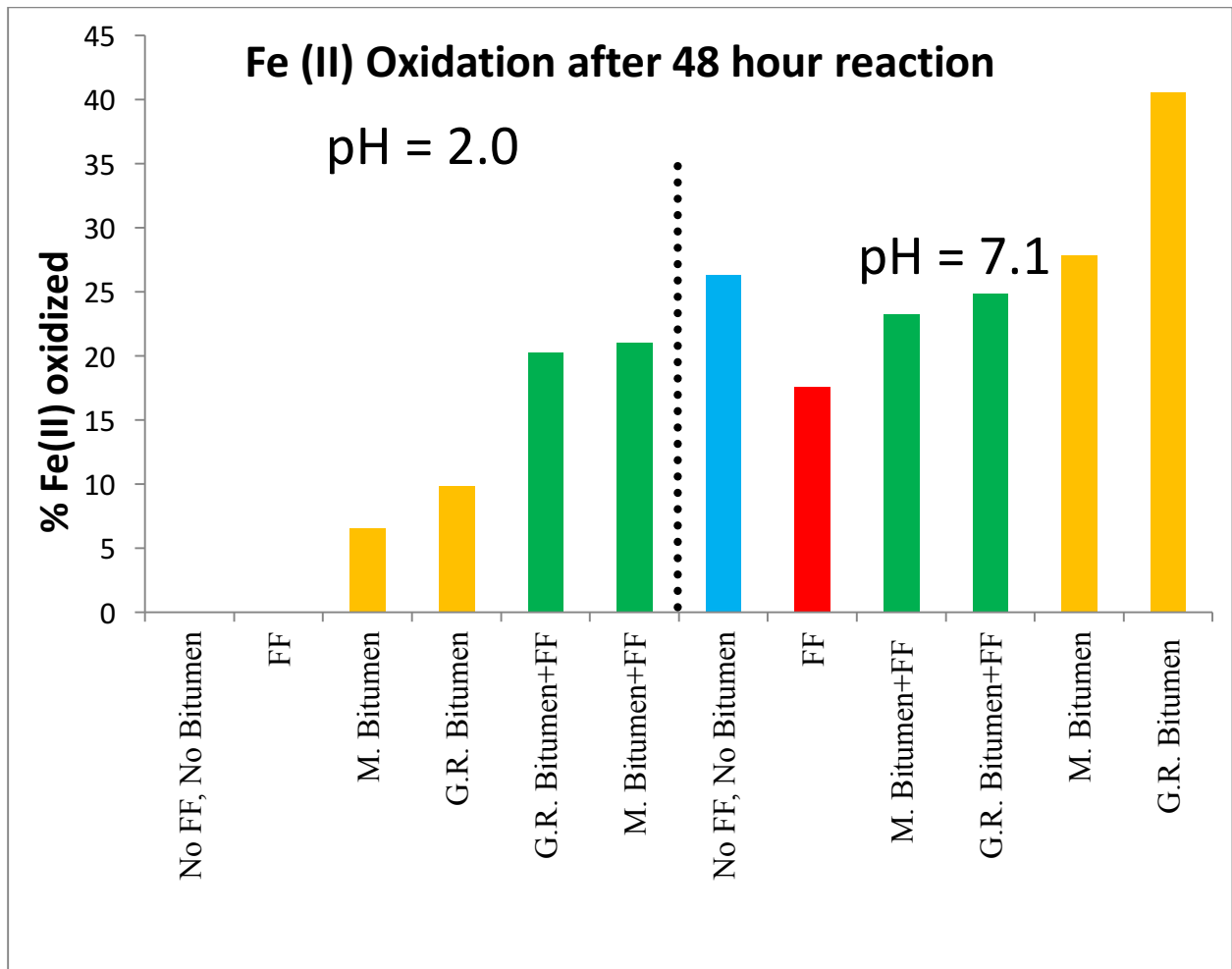
3

4

5

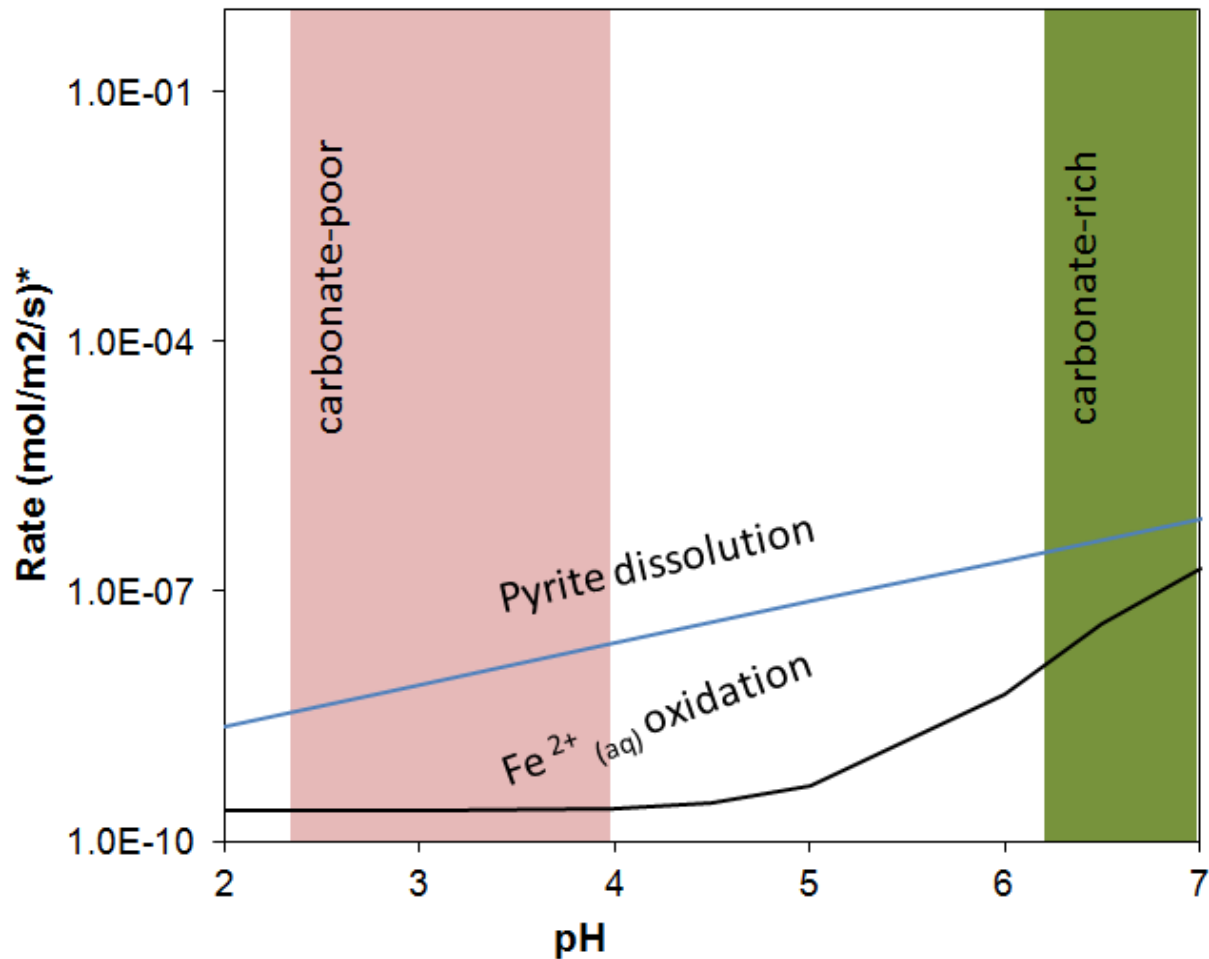
Pathway	CN	R	σ^2
Fe-C	7.45 ± 0.36	2.11 ± 0.02	0.010 ± 0.001
Fe-S	1.93 ± 0.30	3.22 ± 0.01	0.008 ± 0.001
Fe-Fe	1.31 ± 0.21	3.82 ± 0.01	0.005 ± 0.001
E_0	-0.118 ± 0.425	Red Chi sq	7.81
$S0^2$	0.896 ± 0.040	R Factor	0.0294

Figure 9: Shell-by-shell fitting of Fe K-edge EXAFS data for Green River Shale, unreacted. A) Fit of EXAFS data using Fe(II)-C pathway along with the Fe-S and Fe-Fe pathways of pyrite/pyrrhotite. B) Fit of the Fourier Transform.



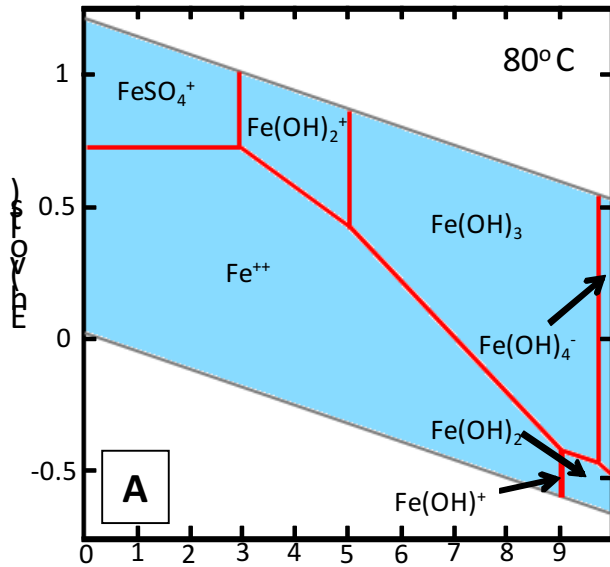
1
2
3
4
5
6

Figure 10: Percentage of Fe(II) oxidized in idealized Fe reactors over a 48 hour period at two different solution pHs with and without the presence of bitumen. FF stands for Fracture Fluid, while M. stands for Marcellus and G.R. stands for Green River.

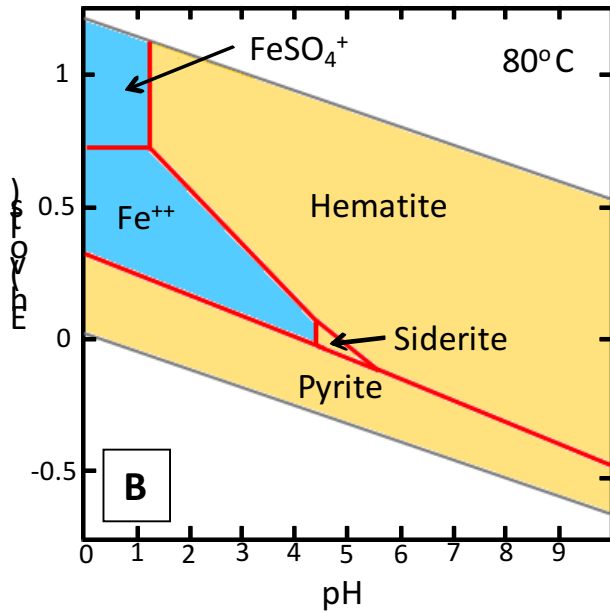


1

2 **Figure 11:** Conceptual diagram of relative rates of pyrite dissolution and Fe(II) oxidation as a function
 3 of pH. Pyrite dissolution rates were calculated using a rate law from McKibben and Barnes⁴⁵ at 30°C
 4 with a fixed Fe(III) concentration of 6.12×10^{-5} mol/L and a rate constant of 3.0 mol/m²/s. Aqueous
 5 Fe(II) oxidation rates were calculated after Morgan and Lahav³⁸ at 20.5°C using a fixed total aqueous Fe
 6 concentration of 2.28×10^{-4} mol/L. The pyrite dissolution and aqueous Fe(II) oxidation rates are in units of
 7 mol/m² mineral/s and s⁻¹ (*), respectively. The pH range encountered by the carbonate-poor and
 8 carbonate-rich shales are indicated by pink-and green-shaded regions, respectively.



1



2

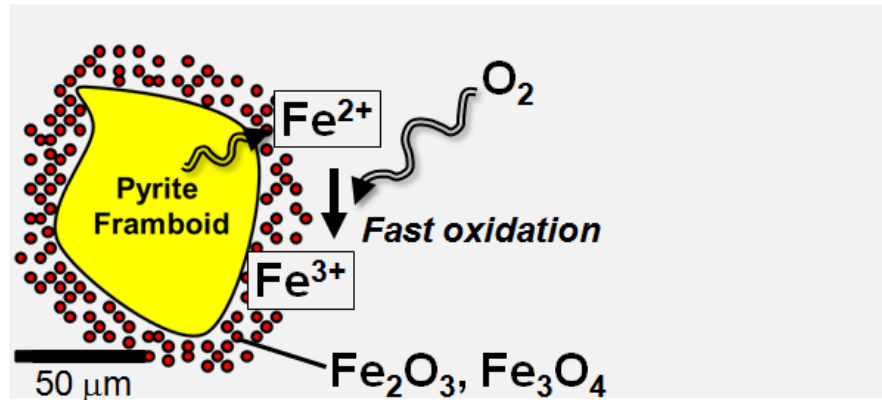
3 **Figure 12:** Eh/pH diagram for the Marcellus shale reactors (Blue denotes aqueous species while Orange
 4 denotes solid species). (A) Diagram of Fe aqueous species, all minerals suppressed. (B) Diagram of Fe
 5 species with no minerals suppressed showing that hematite is the predominant Fe(III)-bearing species at
 6 equilibrium. Diagram parameters: Fe = 4.66×10^{-4} M, Ca = 5.6×10^{-3} M, Mg = 4.94×10^{-4} M, HCO_3^- = $5.6 \times$
 7 10^{-3} M, and SO_4^{2-} = 1×10^{-3} M.

8

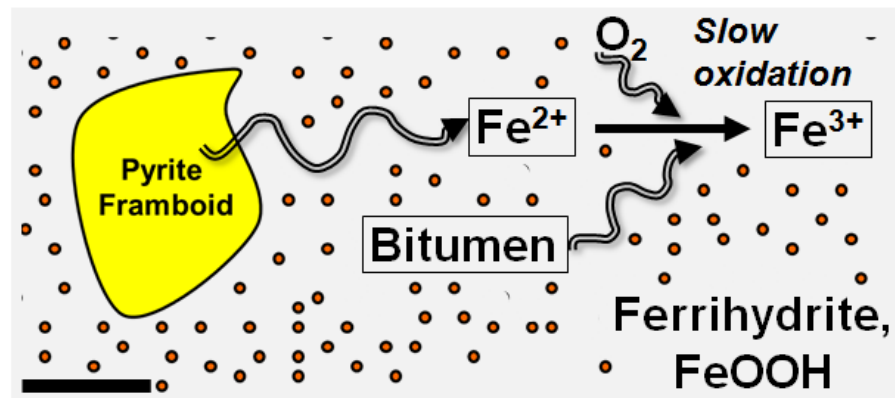
9

1

pH 7



pH < 4



2

3

4 **Figure 13:** Conceptual model of Fe behavior in hydraulic fracturing systems based on solution pH. The
5 pH 7 scenario occurs in systems with high carbonate concentrations or distances far away from the drill
6 bore where injected HCl is neutralized (high carbonate) or very dilute (away from drill bore). The pH < 4
7 scenario is for low carbonate systems or near drill bores where the low pH slows down Fe(II) oxidation.